NJC

New Journal of Chemistry

An international journal of the chemical sciences

www.rsc.org/njc

Volume 32 | Number 8 | August 2008 | Pages 1269–1456

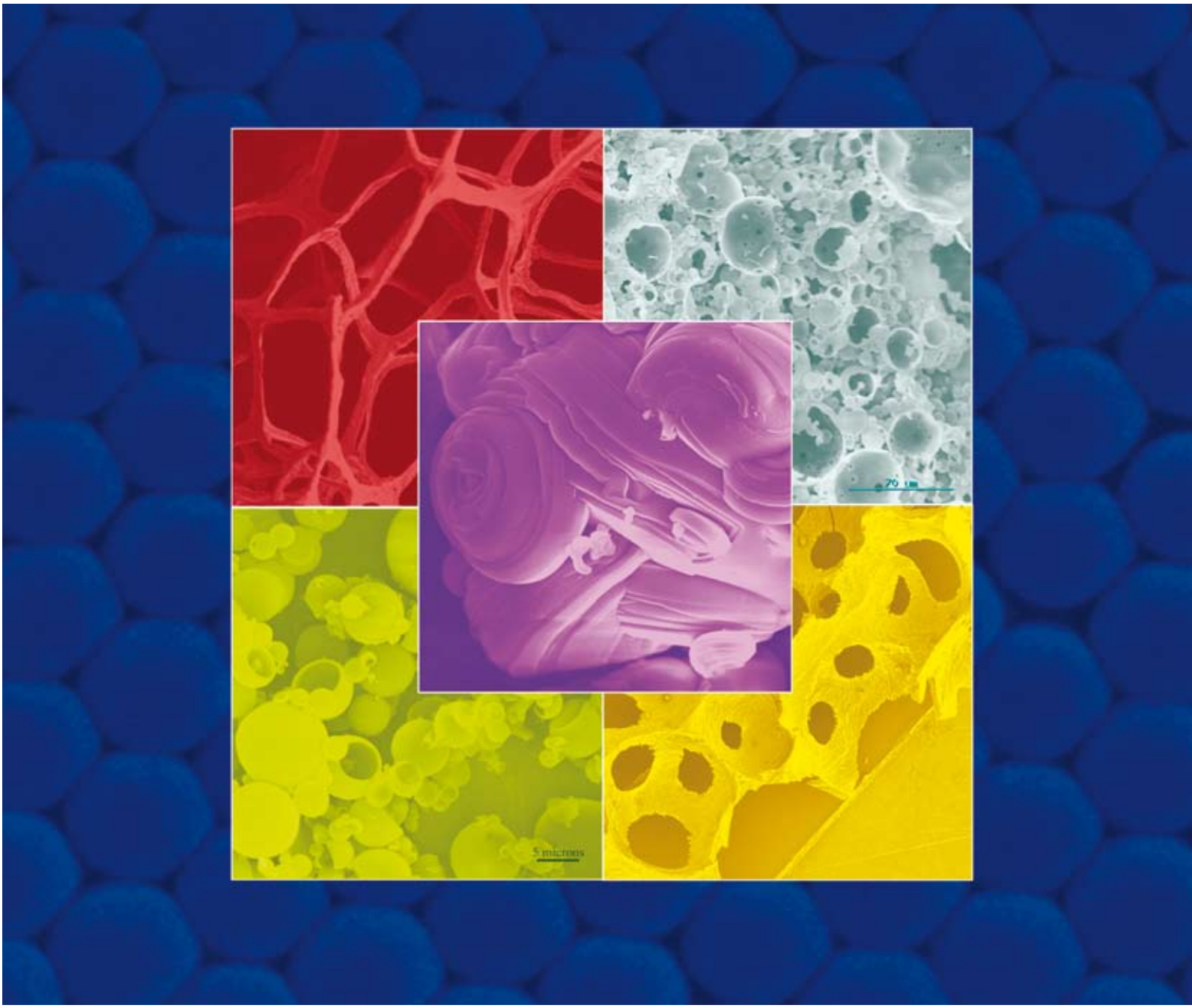

ISSN 1144-0546

RSC Publishing

CENTRE NATIONAL DE LA RECHERCHE SCIENTIFIQUE

PERSPECTIVE

Renal Backov *et al.*

Bio-inspired synthetic pathways and beyond: integrative chemistry

1144-0546(2008)32:8;1-#

Bio-inspired synthetic pathways and beyond: integrative chemistry

Eric Prouzet,[ab] Serge Ravaine,[c] Clément Sanchez[d] and Rénal Backov[c]

Received (in Montpellier, France) 13th February 2008, Accepted 2nd May 2008
First published as an Advance Article on the web 7th July 2008
DOI: 10.1039/b802527b

Herein are described some rational synthetic pathways for generating complex architectures with enhanced application in either optics, catalysis, phase separation or magnetism. The ability of integrative chemistry to scissor condensed matter at several length scales where final objects will be macroscopically one-dimensional (1D), two-dimensional (2D) or three-dimensional (3D) is discussed. In this general context, the first section deals with fibers generated either through electrospinning or extrusion processes bearing, respectively, magnetic and sensor properties. The second part is dedicated to periodic mesostructured thin films (POMTFs) and nanotextured films obtained, respectively *via* EISA and Langmuir–Blodgett techniques, where optical properties will be an issue in both cases through respectively sensing and photo band gap properties. Finally the third part will dedicated to pseudo 3D objects, namely membranes, and 3D mesomacrocellular foams, promoted respectively by mesoscale-driven self organization and emulsion-based synthetic routes where final applications will range from filtration to heterogeneous catalysis.

After briefly discussing some challenges that should be addressed in the future for ''integrative chemistry'', we conclude that it should be seen as an ''interdisciplinary tool box'', being a specific space of freedom where each chemist can express his or her own creativity through a rational approach.

Introduction

Today, in order to satisfy society's high standard technology specific needs, chemical sciences are required to promote and design complex architectures bearing functionalities or information at divers length scales. From the associated chemical synthetic pathways has emerged the notion of ''complexity''[1] in chemical science. For instance, skeleton of such architectures might be exclusively inorganic, organic or hybrid organic–inorganic, biological–inorganic. Furthermore, to this variety in nature might be coupled several textural modes occurring at different length scales, for instance, lyotropic mesophases, foams, extrusion process, preformed nano-building blocks, dip-coating, electrospinning and so forth. The textural modes are only limited by chemists' imagination and creativity. But at that point we can sense that chemical reactions would now operate at low temperatures in order to preserve either the organic counterparts of the architectures or the soft textural modes involved during the synthetic routes. For instance, the integration between the ''sol–gel process'' and ''soft matter'' is a frank success as they can interact together without disrupting their own function, *i.e.* generate a solid network for the former and promote patterning effects

[a] *University of Waterloo, Department of Chemistry, 200 University Avenue West, Waterloo, Ontario, Canada N2L 3G1. E-mail: eprouzet@sciborg.uwaterloo.ca; Fax: (+1) 519-746-0435; Tel: (+1) 519-888-4567 (#38172)*
[b] *Institut Européen des Membranes, IEM UMR 5635, CNRS, 1919 Route de Mende, 34293 Montpellier, France*
[c] *Université Bordeaux I, Centre de Recherche Paul Pascal, UPR CNRS, 8641, 115 Ave. Albert Schweitzer, 33600 Pessac, France. E-mail: backov@crpp-bordeaux.cnrs.fr. E-mail: ravaine@crpp-bordeaux.cnrs.fr; Fax: (+33)-5 56 84 56 00; Tel: (+33)-5 56 84 56 30, (33)-5 56 84 56 57*
[d] *Laboratoire de Chimie de la Matière Condensée de Paris LCMC-P UMR CNRS 7574 Université Pierre et Marie Curie Couloir 54-55 (5ème Etage.) 4, place Jussieu 75252 Paris, Cedex 05, France. E-mail: clement.sanchez@upmc.fr; Fax: (+33)-1-44 27 47 69; Tel: (+33)-1-44 27 55 34*

Eric Prouzet is CNRS Senior Scientist at the European Institute of Membranes (Montpellier, France) and Associate Professor in Chemistry and Nanotechnologies at the University of Waterloo (Canada). His research interests include the synthesis of porous materials and nano-objects with the help of soft matter (micelles, liquid crystals, biogels) towards applications in the domain of membrane processes as well as catalysis.

Serge Ravaine received an engineer diploma from the National School of Chemistry and Physics of Bordeaux in 1991 and a PhD in Physical Chemistry at the University of Bordeaux in 1995. He is currently full professor at the University of Bordeaux and his research interests at the Centre de Recherche Paul Pascal in Pessac (France) include the synthesis of hybrid colloidal particles and the fabrication of three-dimensional colloidal photonic crystals.

Clément Sanchez is Director of Research at the CNRS, head of the ''Chimie de la Matière Condensée de Paris'' laboratory and head of Nanochemistry Division of C'Nano Ile de France. His work includes soft chemistry routes to nanomaterials, sol–gel chemistry of transition metal oxide based materials, templated synthesis of porous and non-porous materials, and bio-inspired approaches to hierarchically structured materials.

Rénal Backov is associate professor at the University of Bordeaux and leads the integrative chemistry and multiscale functional materials group at the Centre de Recherche Paul Pascal in Pessac. His activities encompass the areas of sol–gel chemistry and process, coordination chemistry as well as polymers and physical chemistry of complex fluids.

for the latter. From this interface has emerged the notions of "chemistry of shapes"[2] or "syntheses over all length scales",[3] where bio-inspired materials and the full set of biomimetic approaches[4] still offer a wide scope of opportunities and challenges to transpose or recreate complex and hierarchical architectures[5] obtained through the so-called "integrative synthesis"[4e,6] routes. Nevertheless, if the approaches mentioned above are successful from a "shaping" point of view, the transposition to functional materials bearing both enhanced functionalities and competitive applications with what already exists in the industrial market is low. There is thus a crucial need for a "rational design" of complex architectures where the first parameter to bear in mind is not the "shaping for the shaping" or even the competence and methodology in use, but rather the enhanced function or real competitive application to be reached which will then determine the overall synthetic pathway to be applied. From this way of thinking, and taking into account the first notion of "complexity" in chemical science,[1] has recently emerged the concept of integrative chemistry,[7] which can be defined as an "interdisciplinary tool box" where confined reactors operate at diverse length scales, those reactors acting either in cooperative or independent action modes.[8] The chemical reactions that should still operate at low temperature are indeed not restricted to "sol–gel" chemistry and processing but can be extended to coordination chemistry, supramolecular as well as polymer chemistry. Integrative chemistry concept also encompasses the "green chemistry" of bio-inspired materials and systems and it should provide breakthroughs in the design of advanced materials as many existing solutions are becoming limited with regard to new technical, economic or ecological developments and demands.[9]

Herein we would like to describe non-exhaustive rational synthetic pathways where the final architectures bear enhanced application either in optics, catalysis, phase separation or magnetism. We aim to propose herein as a guideline the abilities of integrative chemistry to scissor condensed matter on several length scales where final objects will be macroscopically one-dimensional (1D), two-dimensional (2D) or three-dimensional (3D). In this general context, the first section will deal with fibers generated either through electrospinning or extrusion processes bearing respectively magnetic and sensor properties. The second part will be dedicated to periodic mesostructured thin films (POMTFs) and nanotextured films obtained, respectively *via* evaporation induced self assembly (EISA) and Langmuir–Blodgett techniques, where optical properties will be an issue in both cases through respectively sensing and photo band gap properties. Finally the third part will dedicated to pseudo 3D objects, namely membranes, and 3D mesomacrocellular foams promoted respectively by mesoscale-driven self organization and emulsion-based synthetic routes where final applications will range from filtration to heterogeneous catalysis.

Overall, the goal of this illustrated discussion is certainly not to be exhaustive regarding mentioning all the synthetic pathways that permit the generation of hierarchical architectures, but rather to show that through integrative chemistry rational design it is possible to reach complex architectures bearing specific, new or enhanced properties.

1-Dimensional (1D) object generation: fibers and application in magnetism and sensors

Example of fibers bearing magnetic properties obtained through electrospinning

Recent interest in jet-based technologies has escalated exponentially as these techniques increasingly show great promise for handling materials on a scale ranging from the molecular level, in both the chemical and biological sciences, to micro- and nanosized suspensions used in materials science and engineering. There are a number of different jet-based methodologies capable of handling this diversity of materials, namely, ink-jet printing (IJP),[10a,b] electrospraying,[11] and electrospinning.[12] These shaping techniques are particularly attractive for generating 1D materials. In the past decade, more and more attention has been drawn to the fabrication of one-dimensional (1D) nanomaterials, including nanotubes, nanowires, nanofibers, and nanobelts because they show some distinctive properties compared with bulk materials.[13] Particularly, 1D magnetic nanomaterials are expected to have interesting properties, as the geometrical dimensions of the material become comparable to key magnetic length scales, such as the exchange length or the domain wall width.[14] Electrospinning is therefore appearing as a simple and effective method for fabricating ultrathin nanofibers, either oriented or laid in a random fashion.[15] In a typical electro-spinning setup, high voltage is applied to a droplet of polymer solution that rests on a sharp conducting tip. As a result of molecular ionization and charge redistribution, a Taylor cone is formed and a jet of the solution is extracted. The formed jet is then accelerated by the electric field and collected on a grounded substrate. When a volatile solvent is used, in-flight solvent evaporation occurs, hardening the fibers composed of the dissolved material, which are deposited on the substrate. With this technique, fibers have been electrospun from a wide variety of polymers.[16] In addition to polymer nanofibers, ceramic, composite, and carbon nanofibers can be fabricated using this simple technique. For example, oxide nanofibers such as ZnO, TiO_2, NiO, and CuO have been prepared by calcination of electrospun nanofibers containing polymer and inorganic precursor.[15e–g] Also, for fabricated assembled nanofibers as uniaxially aligned arrays, a modified electrospinning setup was employed.[15a] It is essentially the same as the conventional configuration except for the use of a collector containing a gap with a width of 1 mm in its middle. Such a collector was simply fabricated by putting two silver plates in a side-by-side parallel arrangement (Fig. 1). Aligned arrays of the electrospun nanofibers can be collected on the gap; the fibers were then transferred onto a silicon wafer for further heat treatment. Single nanofibers of Fe, Co, and Ni suspended across the small gap can also be obtained with a short collection time of about 10 s.[17]

After applying the shaping process, Fe, Co, and Ni nanofibers could be obtained by very carefully deoxygenizing Fe_2O_3, CoO, and NiO nanofibers through applying a hydrogen atmosphere at 400 °C for 1 h.[17] Wu *et al.*[17] characterized the magnetic properties of the synthesized nanofibers using a vibrating sample magnetometer (VSM). Fig. 2 shows the

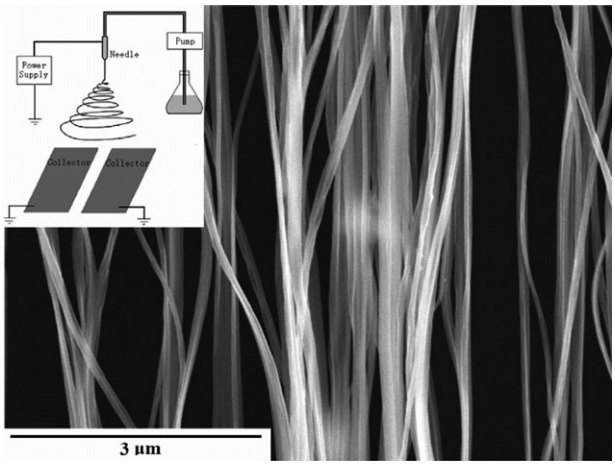

Fig. 1 SEM image of a uniaxially aligned array of Ni nanofibers that were prepared using two parallel electrodes as fiber collector. Inset is the schematic illustration of the setup for electrospinning that was used to generate uniaxially aligned nanofibers. The collector contained two pieces of conductive silicon separated by a gap (ref. 17, copyright 2007 American Chemical Society).

room-temperature magnetization hysteresis loops of (a) Fe_2O_3, (b) CoO, and (c) NiO nanofibers and their corresponding metallic nanofibers.

It can be observed that the hysteresis curves of Fe, Co, and Ni nanofibers revealed typical ferromagnetic behaviors, whereas the curves of Fe_2O_3, CoO, and NiO nanofibers show nearly a flat line with low magnetization. The ferromagnetism of Fe, Co, and Ni nanofibers is clearly demonstrated by coercivity (H_c), saturation magnetization (M_s), remanent magnetization (M_r), and saturation field (H_s).[17] The room-temperature saturation magnetizations of Fe, Co, and Ni nanofibers are 91.74, 69.22, and 24.76 emu g^{-1}, respectively, which are about half of the value of corresponding bulk metals (Fe, 221.71 emu g^{-1}; Co, 162.55 emu g^{-1}; and Ni, 58.57 emu g^{-1}.[18] A saturation magnetization lower than that for bulk materials is normal for nanomaterials.[19] Typical reasons for this include the oxidation of the surface of magnetic nanofibers, which may create a magnetically dead layer. The large specific area and the imperfection of the crystalline structure at the surface may also lead to a significant decrease in the nanofiber saturation magnetization. It is important to note that the synthesized magnetic metallic nanofibers exhibit great enhanced coercivities, which are about 2 orders of magnitude higher than that of bulk materials. The coercive fields obtained in the Fe, Co, and Ni nanofibers were 427, 651, and 124 Oe; whereas those of bulk Fe, Co, and Ni are only 1, 10, and 0.7 Oe, respectively.[18,20] The enhancement of coercivity may be attributed to the single-domain nature and anisotropic shape of the nanowires.[21] A higher coercivity is a key factor for information storage, although real devices also require intensive studies on magnetization interaction, local magnetization reversal characterization, and other important issues. Nevertheless, such novel magnetic nanofibers are of potential interest for high-density information storage application. Additionally, because the magnetic coercivities of the nanofibers are outstanding and the synthetic method is low cost and highly efficient, bulk amounts of randomly oriented ferromagnetic metal nanofibers could also be used for manufacturing flexible magnets after blending different loads with polymers.

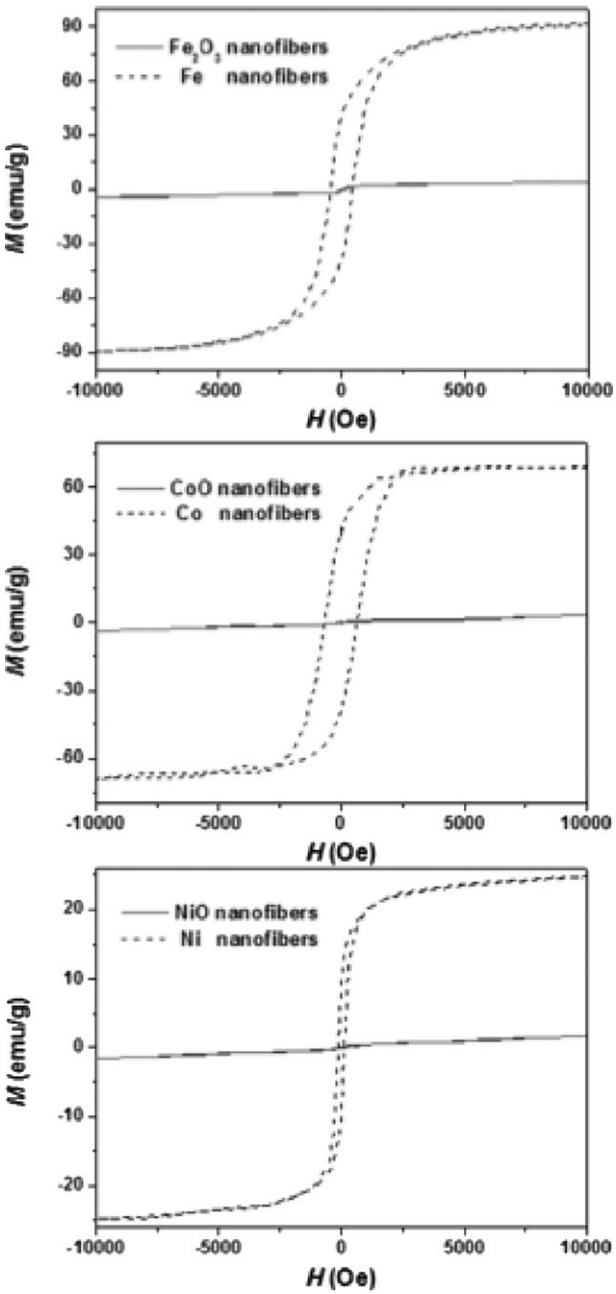

Fig. 2 Magnetic properties of the electrospun nanofibers before and after being annealed in a hydrogen atmosphere: (a) magnetic hysteresis loops for Fe_2O_3 nanofibers (solid line) and Fe nanofibers (dashed); (b) CoO (solid) and Co nanofibers (dashed); (c) NiO (solid) and Ni nanofibers (dashed). The measurements were conducted at room temperature, with the applied magnetic field parallel (in-plane) to the nanofiber film surface (ref. 17,copyright 2007 American Chemical Society).

Example of fibers bearing sensor properties obtained through extrusion process

The extrusion process can be adapted to promote coaxial flow from which one-dimensional (1D) nanotextured materials

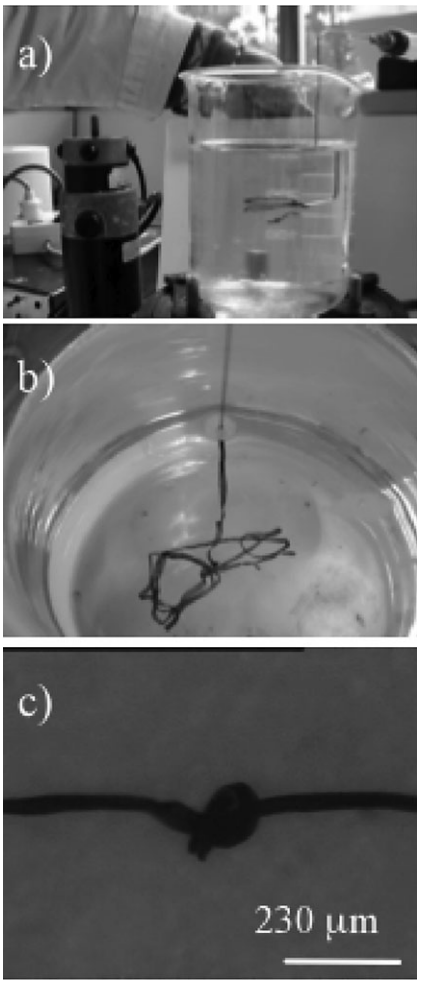

Fig. 3 (a) Vanadium oxide sol injection step, (b) vanadium oxide fiber extraction from the PVA solution, (c) final fibers forming a knot (ref. 22, copyright 2005 Wiley-VCH).

have been generated to produce a new semi-conducting gas sensor.[22] In this regard, the V_2O_5 fibers presented in this study appear as good candidates to assess sensing applications. From the extrusion process described in detail elsewhere,[22] vanadium oxide macroscopic fibers can be obtained (Fig. 3).

Upon the extrusion process in use, final vanadium oxide fibers depict a good transversal flexibility that allows knot formation (Fig. 1c). In order to assess the longitudinal mechanical properties, traction measurements have been performed (not shown here), and we found out that they do not possess plastic behavior before they break. This demonstrated that the vanadium oxide nanoscopic ribbons, constituting the macroscopic fiber nanobuilding blocks, are strongly packed together thus avoiding any longitudinal displacement. Considering both transverse flexibility (Fig. 3c) and the quasi-absence of longitudinal plasticity those fibers depict anisotropic mechanical properties. In the elastic regime, at low deformation, the longitudinal Young's modulus of the fibers varies from 12 to 17 GPa, values that correspond to those obtained for carbon nanotube macroscopic fibers.[23] These vanadium oxide fibers also show high scale textural anisotropy as revealed when performing cross-polarized microscopy, TEM and SAXS experiments (Fig. 4).

We can observe (Fig. 4a) that the transmitted light intensity is optimum when the fiber main axis is placed at 45° between the two polarizers. The birefringence depicted in Fig. 4a demonstrates that preferential orientation has been generated within those fibers. TEM observations reveal that nanoscale ribbon subunits are effectively organized preferentially parallel to the macroscopic fiber main axis (Fig. 4b). In Fig. 4b we notice that the nanoscopic objects constituting the fibers are made of very thin ribbons that statistically fold to themselves along their main axis. Overall, this high scale anisotropic configuration of the nanoscopic vanadium oxide ribbons is certainly induced by the extrusion process where a strong shear is imposed on the gel outflow when injected into the

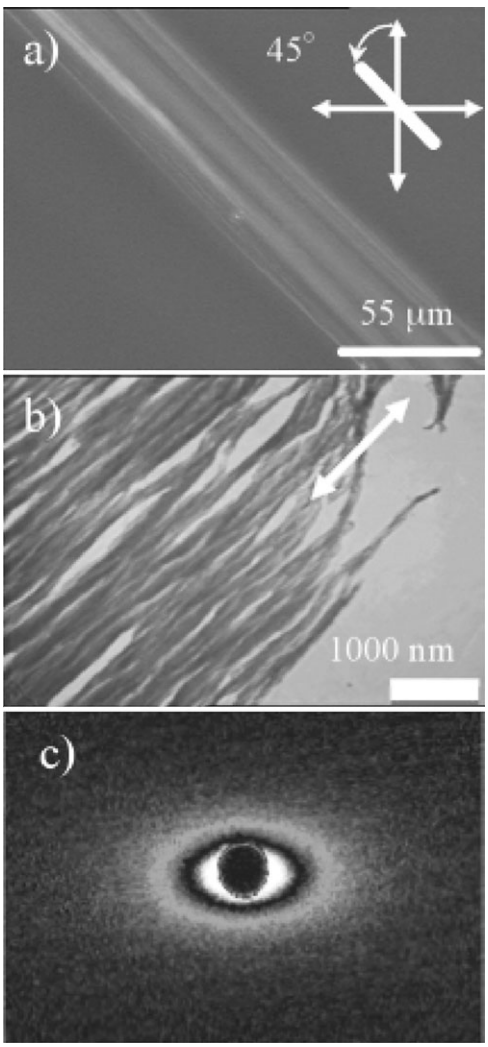

Fig. 4 (a) Vanadium oxide fibers observed through cross-polarized microscopy. The scale bar represents 55 μm (the top right schemes depict the cross-polarizers (double white arrows) while the fiber main axis is represented with the superimposed white bold line). (b) TEM observations performed on vanadium oxide fibers (the white double arrow indicates the macroscopic fiber main axis. Fiber thicknesses have been minimized using an electron beam degradation process). (c) Anisotropic SAXS pattern of a fiber with the main axis vertical (ref. 22, copyright 2005 Wiley-VCH).

PVA solution. More recently we were able to tune the shear rate while performing the extrusion by varying the needle position within the rotating beaker. As a direct consequence both sensors and mechanical properties were varied and controlled with rational design.[22b] In order both to assess this preferential orientation and avoid any fiber degradation, induced by the electron beam used for the TEM observation, we performed SAXS experiments on as-synthesized fibers (Fig. 4c). In Fig. 4c we can observe an anisotropic diffuse spot around the beam trap. The diffuse spot is more extended along the horizontal direction. Since the fiber axis is vertical, the vanadium oxide ribbons, on average, have their long axis vertically aligned, as demonstrated through TEM observations (Fig. 4b). In fact this high scale preferential orientation should be strongly related to the following parameters: the difference between the speed associated with the syringe vanadium oxide outflow and the rotational speed imposed on the beaker containing the PVA solution, and also the difference in viscosity between the vanadium oxide sol and the PVA solution should be taken into account. The relation between those parameters and final large scale preferential orientation of the nanoscopic ribbons is currently under way. To assess the vanadium oxide fiber microstructure we performed both XRD experiments using reflection geometry, ^{51}V MAS NMR spectroscopy and ESR measurements (not shown here). Overall, those microstructure characterizations reveal an amorphous character that is locally similar to the $V_2O_5 \cdot 1.8H_2O$ xerogel.[24] Concerning the sensor applications, the cells (Fig. 5) allow measurement of the distance of the fiber between the two gold electrodes (L) while their surface diameter has been previously measured using an optical microscope (S). As we can check the system resistance (R) using a multimeter, the conductivity can obviously be calculated ($\sigma = L/(RS)$).

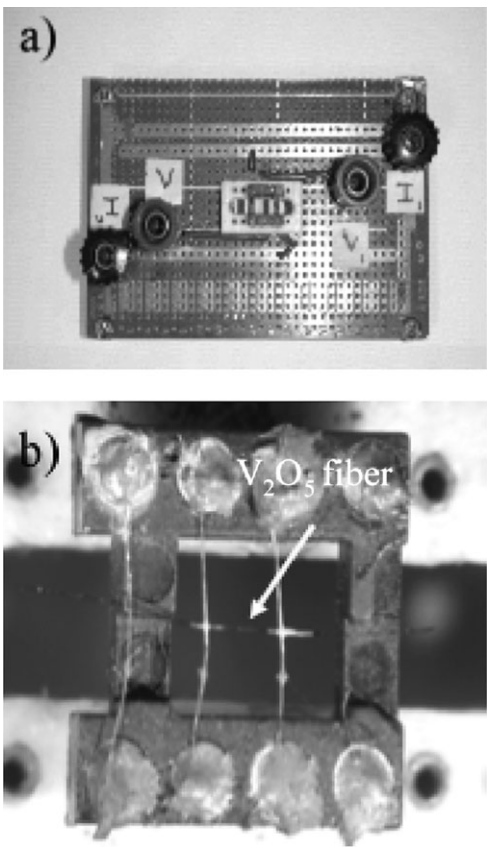

Fig. 5 Conductivity cell made with a single vanadium oxide fiber (ref. 22*b*, copyright 2005 Wiley-VCH).

We have first checked the as-synthesized sensor responses toward different methanol vapor sources (Fig. 6a). Considering Fig. 6a–d we can observe that conductivity isotherm responses cycle when the vanadium oxide sensing experimental set-up is exposed to or subsequently removed from the alcohol vapor source and the conductivity turn over occurs instantaneously. Secondly, we investigate the sensor selectivity (Fig. 6e). We can observe in Fig. 6e that the increase and decrease of conductivity are strongly related to the nature of the alcohol, which results in specific signal shape, the shape of the specific signals acting as a direct signature of the alcohol nature, providing thus the selectivity criteria.

Considering Fig. 6b, the conductivity value reached for methanol is in the same range as that obtained for ethanol, but those values decrease drastically when propanol or pentanol is used as the vapor source. A conductivity mechanism has been hypothesized elsewhere[25] in terms of surface charge electron-depletion strongly associated with the O–H bond ionic character. Considering the alcohols used in this study, the donor induction effect over the oxygen is diluted when going from methanol to pentanol, minimizing thus both the O–H bond ionic character (or essentially the acidity) and thus the associated conductivity. Beyond cycling signals and their associated selectivity of shape, it is important to appreciate the sensitivity of the vanadium oxide fiber sensors. Also we noticed that a single vanadium oxide fiber can detect down to 0.1 ppm within 16 seconds, a detection time that decreases to 7 seconds for 100 ppm.[23a] This experiment demonstrates the very high sensitivity of the vanadium oxide sensing fibers obtained in this study. Also, these vanadium oxide fiber sensing-cells are still active after several weeks of work. Furthermore, it is important to mention that the present working-temperature is 40 °C which is far lower than those reported in other studies, where sensing effects over ethanol gas sources were conducted between 150 and 400 °C.[25]

2-Dimensional (2D) object generation: films and application as sensors and photonic band gap device

Example of mesoporous thin films bearing sensing properties obtained through EISA process

Periodically organized mesoporous thin films (POMTFs)[7c] are net shaped and present advantages in both facilitating the integration of matter and in the miniaturization of materials and devices. The first POMTFs were processed, respectively, by Anderson *et al.*[26] Ogawa,[27] Ozin *et al.*,[28] and Brinker *et al.*[29] and consist of mesoporous layers of amorphous silica or organosilicas. The field of nonsilicate, transition metal oxide, rare earth, and multimetallic oxide based POMTFs has exploded very recently.[30] Among the methods in use to generate such structured films, the chemical solution deposition methods are the most employed.[29] In this approach, the

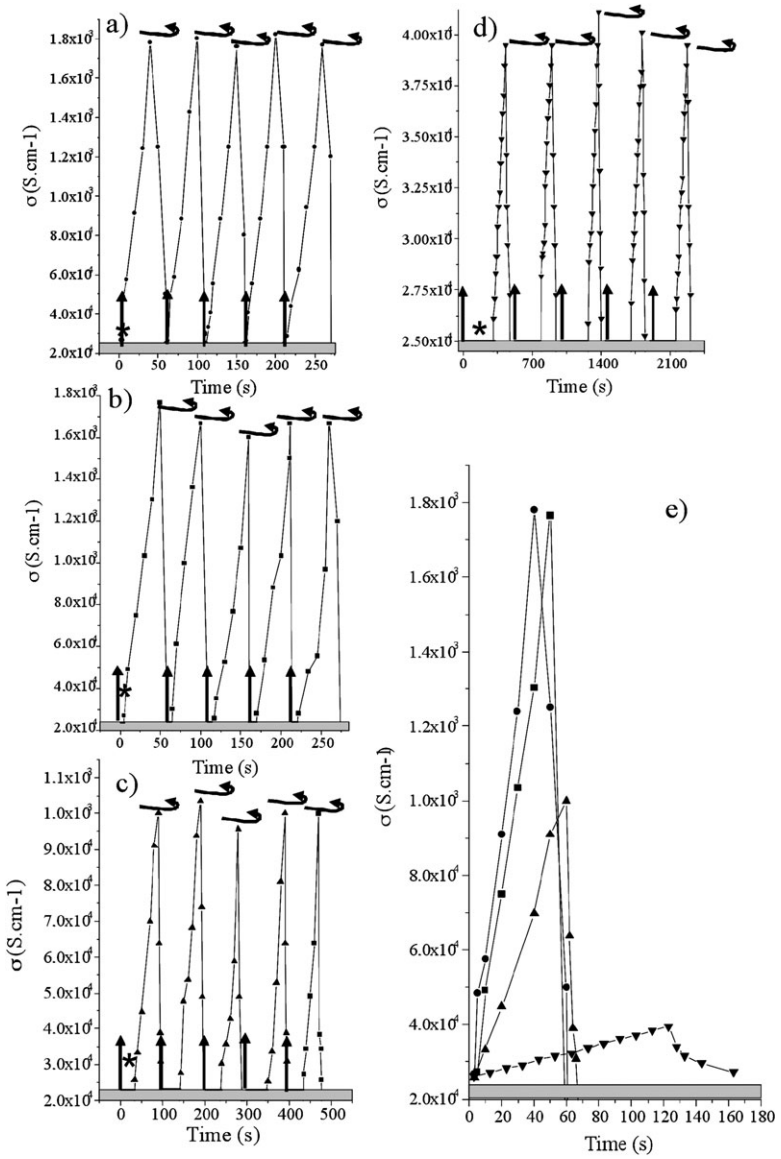

Fig. 6 Typical isotherm response curves on cycling, using different alcohol vapor sources at 40 °C. (a) Methanol, (b) ethanol, (c) propanol, (d) pentanol (the straight black arrows indicate when the sensing cell is exposed to alcohol vapor source), * time response (the curved black arrows indicate when the sensing cell is removed from the alcohol vapor source), (e) specific signal shapes with different alcohol vapor sources: ● ethanol source, ■ methanol source, ▲ propanol source, ▼ pentanol source. The grey part at the bottom of each graph indicates that the multimeter in use is overloaded for high resistivity (from ref. 22*a*, copyright 2005 Wiley-VCH Verlag GmbH & Co. KGaA).

meso-ordering occurs through the evaporation induced self-assembly (EISA) mechanism. Other less developed processes have been also used as for instance, film growth by electrochemical techniques[31]or at air–solution or substrate–solution interfaces (ASI or SSI, respectively).[28a,32] Indeed, these 2D compounds have already found applications in a wide range of domains (*e.g.*, separation techniques, sensors, catalysis, modified nanoelectrodes, nanopatterning of composites, fuel cells, batteries, photovoltaic cells, micro-optics and photonic devices, microelectronics (low *k*), nanoionics, cells, functional, protective coatings, and so forth).[7c] Films and membranes of versatile chemical compositions bearing hierarchical porosity from nanometres to microns can also be processed *via* multiple templating or by coupling nanobuilding block and breath figure approaches. To expand the range of accessible properties, various organic functional groups have been covalently incorporated onto the pore surfaces of mesoporous materials. However, these modifications have provided mainly "passive" functionality, such as controlled wetting properties, reduced dielectric constants, or enhanced adsorption of metal ions. By comparison, materials with "active" functionality would enable properties to be dynamically controlled by external stimuli, such as pH[33] temperature,[34] or light.[34] In particular, the Brinker group[34] reported the synthesis of nanocomposite POMTFs functionalized with photoresponsive azobenzene-containing organosilanes. Azobenzene derivatives were selected because their *trans* to *cis* isomerization is UV sensitive. UV irradiation of the *trans* isomer causes transformation to the *cis* isomer. Removal of the UV radiation, heating, or irradiation with a longer wavelength switches the system back

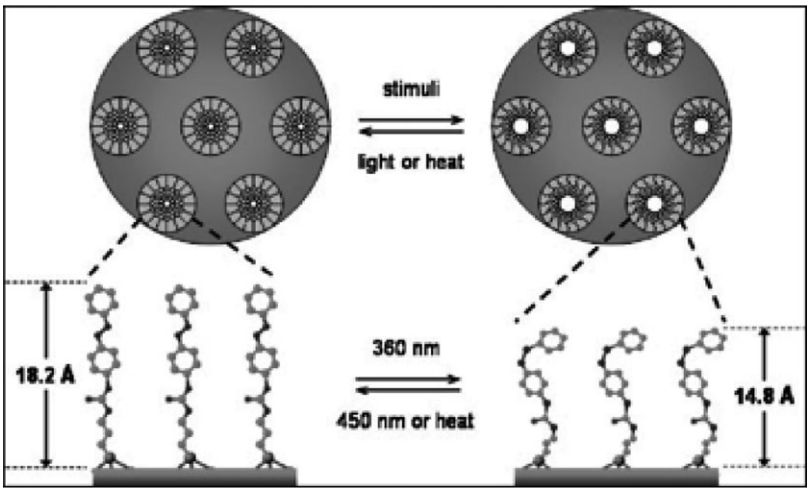

Fig. 7 Photoresponsive nanocomposites prepared by EISA. (ref. 34*b*, copyright 2003 Wiley-VCH).

to the *trans* form. This isomerization changes the molecular dimensions of the organic molecule (the molecular length of the *cis* isomer is shorter than that of the *trans* isomer, Fig. 7).

To demonstrate optical control of mass transport, chronoamperometry experiments were performed using an electrochemical cell working electrode modified with an azobenzene-functionalized nanocomposite membrane (Fig. 8a).[34*a*]

The chronoamperometry experiment used ferrocene dimethanol (FDM) and ferrocene dimethanol diethylene glycol (FDMDG) as electrochemical probes and provided measurement of mass transport properties through the nanocomposite hybrid membrane (Fig. 8c). During electrolysis at constant potential, the effective pore size limits the diffusion rate of probing molecules to the electrode surface. Under dark conditions, the azobenzene moieties are predominantly in their extended *trans* form. Upon UV irradiation (λ = 360 nm), azobenzene moieties isomerize to the more compact *cis* form which increases the diffusion rate and, correspondingly, the

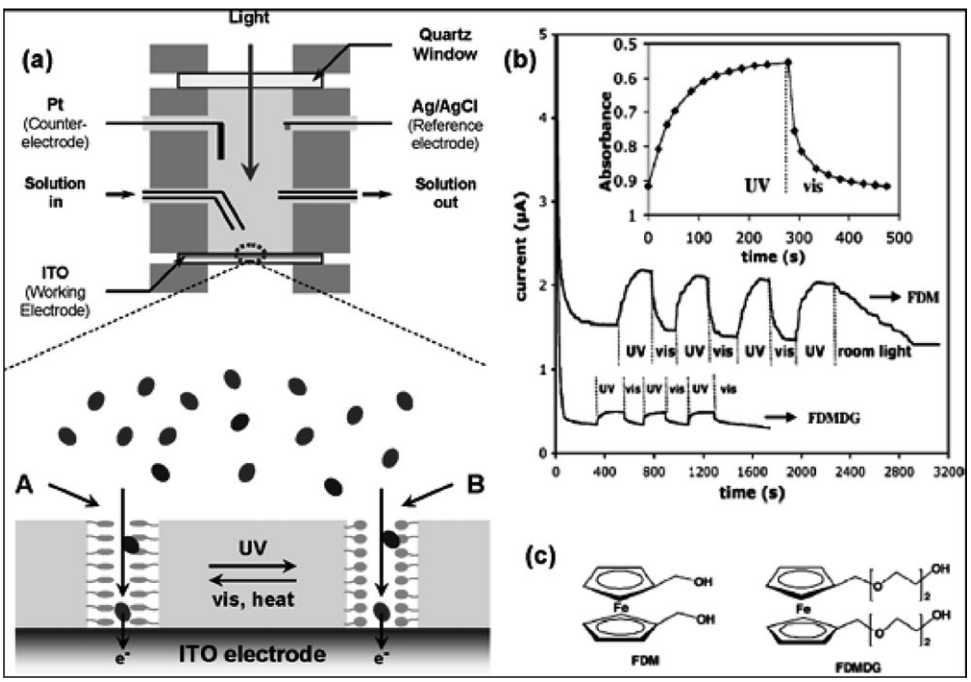

Fig. 8 (a) Schematic drawing of the electrochemical cell (top) and mass transport of probing molecules through the photoresponsive nanocomposite membrane integrated on an ITO electrode (bottom). (A) Diffusion through smaller pores with azobenzene ligands in their *trans* configuration; (B) diffusion through larger pores with azobenzene ligands in their *cis* configuration. Legend: Big ovals represent both neutral and cationic FDM and FDMG species. Small ovals represent azobenzene in *cis* form, while small elongated ones represent azobenzene in *trans* form. (b) Current–time, *I*–*t*, behavior of a photoresponsive nanocomposite film under alternate exposure to UV (360 nm) and visible light (435 nm). (Last cycle uses room light, 400–700 nm.) Inset is the absorbance at 356 nm (π–π^* transition of the *trans* isomer) of the same film immersed in the buffer solution containing 1 mM FDM. (c) Electrochemical probes: ferrocene dimethanol (FDM) and ferrocene dimethanol diethylene glycol (FDMDG) (ref. 34*a*, copyright 2004 American Chemical Society).

oxidative current (Fig. 8b). Likewise, exposure to visible light (435 nm) triggers the reverse *cis–trans* isomerization of the azobenzene moieties, which decreases the current to the pre-UV exposure level. Moreover, it was observed that increasing the volume of the diffusing analyte decreased the overall mass transport, leading to some selectivity for this nanocomposite.

Examples of nanostructured films bearing photonic bandgap properties obtained through the Langmuir–Blodgett technique

Photonic bandgap (PBG) crystals are spatially periodic structures constructed from alternating regions of dielectric materials with different refractive indices.[35] Because of its periodic modulation in dielectric constant, a PBG crystal is capable of controlling the propagation of photons in much the same way as a semiconductor does for electrons: that is, there exists a forbidden gap in the photonic band structure that can exclude the existence of optical modes (within a specific range of frequencies) inside the periodic lattice. Consequently, periodicity can generate optical operations such as mirror or filters. The basic idea of the extension of the periodicity towards a periodicity greater than 1 is to provide omnidirectional reflectors or filters or even more to create very sharp efficient waveguides, new types of highly efficient couplers, *etc*. In summary, it would permit to access to a new generation of optical components. Different technological methods have been tested to fabricate PCs. The top-down fabrication approach generally uses photolithography, etching methods, holographic techniques to design periodic structures in monoliths. 2D PCs are quite easily obtained. However, 3D photonic structures benefit from a less mature technology. In fact, at the current stage of development, there still remains a great challenge in applying the conventional patterning techniques to the generation of pre-designed, 3D periodic lattices that will meet all the criteria required for creating photonic bandgaps, especially as these move towards the visible or ultraviolet regions.[36] In these regions, one will need to pattern the dielectric materials into microstructures of 100–300 nm in size along all three dimensions, and to accomplish registration among these structures in different layers with an accuracy of better than tens of nanometres. Among all the alternative methods for 3D patterning, a promising solution consists in using a bottom-up approach in which pre-designed monodisperse building blocks (*e.g*., colloidal objects) are organized into a relatively stable (often long-range ordered) structure through non-covalent interactions.[37] The final structure is usually determined by the characteristics (topologies, shapes, and/or surface functionality) of the building blocks.

Several techniques have been used so far to get 3D PCs starting from colloidal—mostly spherical—particles such as sedimentation,[38] vertical deposition,[39] or spin-coating.[40] Even if 3D photonic structures with a good crystalline quality, also called colloidal crystals, can be obtained, a perfect control of their global thickness is hard to achieve by using these methods. We have demonstrated that the Langmuir–Blodgett (LB) technique[41] is a promising tool in order to elaborate colloidal crystals of silica particles with a well-defined thickness over large dimensions.[42,43] Here we would like to demonstrate that this technique allows inserting one or two monolayers of spheres of different size, which behave as planar defects, inside colloidal crystals. Such defects enable the existence of localized states for photons within the band gap. Fig. 9a shows the SEM side view of a "sandwich" structure made of one monolayer of 510 nm silica particles, which was embedded thanks to the LB technique between a bottom and an upper stack of five and six layers of 360 nm polystyrene (PS) particles, respectively.

Both the defect layer and the good crystalline quality of the heterostructure can be seen on the SEM image. To probe the existence of a defect mode, the sandwich structure was studied using NIR spectroscopy, the results of which are shown in Fig. 9b. It can be seen that even if the refractive index of silica

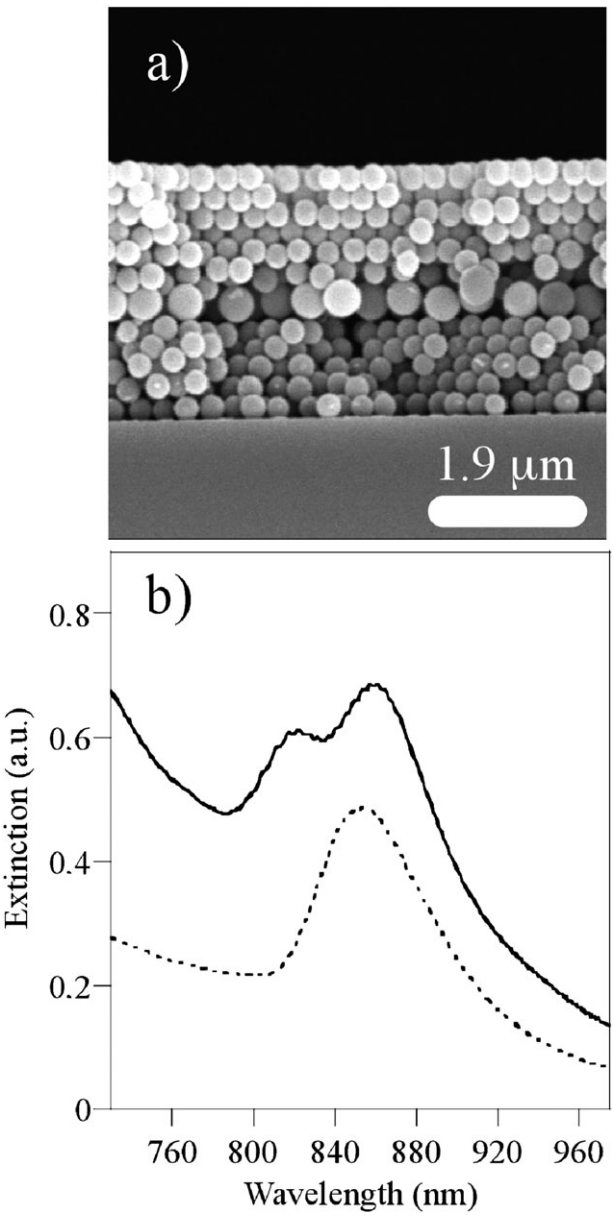

Fig. 9 (a) SEM side view of one monolayer of 510 nm silica particles embedded between a bottom and an upper crystal made of 5 and 6 layers of 360 nm PS particles, respectively. (b) NIR transmission spectra of 10 layers of 360 nm PS particles (dashed line) and of the sandwich structure shown in Fig. 1a (continuous line).

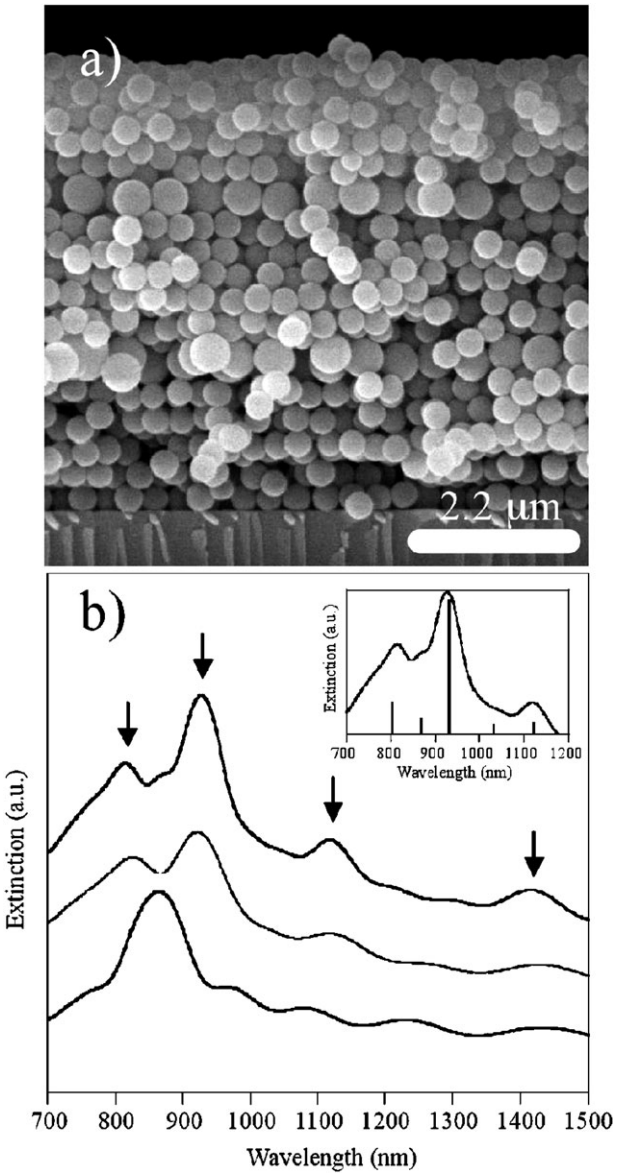

Fig. 10 (a) SEM side view of an $A(BA)_2$ colloidal photonic crystal. (b) NIR transmission spectra of 20 layers of 390 nm silica particles, $A(BA)_1$ and $A(BA)_2$ heterostructures (from bottom to top). The curves have been vertically shifted for clarity. The inset shows an enlargement of the pseudo-gap region of the spectrum of the $A(BA)_2$ heterostructure and a stick spectrum which represents the Fourier transform of the lowest-order approximation to the spatially varying dielectric function, as described in the text.

(n_{Silica} = 1.43(12)) is lower than that of PS (n_{PS} = 1.58(13)), the insertion of a layer of large silica spheres between two opals of smaller PS gives rise to a donor mode, which appears closer to the low-wavelength edge of the gap (*i.e.* around 835 nm). Our capability to build 3D colloidal crystals in a controlled manner was further exploited to fabricate materials presenting two periodically distributed planar defects. Fig. 10a shows a SEM side view of an $A(BA)_2$ heterostructure.

Each A substructure consists of five layers of 390 nm silica particles and presents a highly ordered organization. The overall thickness of the material is uniform despite the presence of defect layers B of larger (590 nm) silica particles which periodically separate the A substructures. The periodic alternation between A and B substructures gives rise to a superlattice, whose periodic parameter corresponds to the sum of the thicknesses of stacks A and B. Fig. 10b shows the NIR transmission spectra of the $A(BA)_1$ and $A(BA)_2$ heterostructures and of a crystal made of 20 layers of 390 nm silica particles. In the case of the ABA heterostructure, a pronounced dip appears inside the original stop-band of the defect-free opal, as it has been already shown.[44] As the ratio of the diameters of guest and host silica particles is close to 1.5, the defect mode is located at the middle of the pseudo-gap.[45] The stop bandwidth is larger than in the case of the defect-free opal. Similar behaviour was previously reported in the literature for donor impurity cases.[46] In order to model the optical behavior of the heterostructures, we have considered that the spectral positions of the reflectivity peaks of such materials can be found from the lowest-order Fourier component of the spatially varying dielectric function. We assumed that the lowest-order approximation to the dielectric function $\varepsilon(x)$ can be written as $\varepsilon_0 \cos(2\pi x/d_A)$ within the A substructures and $\varepsilon_0 \cos(2\pi x/d_B)$ within the B substructures, where ε_0 is the average dielectric constant of the crystals and d_A, d_B are the (111) lattice spacings for the A and B substructures, respectively.[47] As shown in the inset of Fig. 10b, a good agreement between theoretical and experimental spectra is obtained. Moreover, the average spacing between the peaks present at nearly the same wavelength in the curves of the $A(BA)_1$ and $A(BA)_2$ heterostructures (indicated by arrows in Fig. 10b) is proportional to the repeat distance of the superlattice Γ, according to: $\Delta\nu = c/2n_0\Gamma$,[48,49] where c is the speed of light and n_0 is the average refractive index of the crystal. From the Fourier transform of the $A(BA)_2$ structure, we thus can calculate a value of Γ equal to 2.53 µm, which is found to be close to the theoretical one calculated by assuming that it is the sum of the thickness of one A substructure and of one B substructure, *ca.* $\Gamma = 390(4\sqrt{2/3}+1) + 590\sqrt{2/3} = 2.15\,\mu m$. This result shows that the superlattice periodicity modifies the original photonic band structure by opening up the news gaps pointed by the arrows.

3-Dimesional (3D) objects generation: hierarchical porous monoliths bearing selective filtration and heterogeneous catalysis properties

Example of hybrid membrane hierarchically organized obtained through mesoscale-driven self organization

Membranes are semipermeable barriers that allow selective diffusion between two phases. This selective diffusion can arise only from steric retention, which explains why the transport properties of membranes depend first on the membrane microstructure, including pore size, shape, morphology as well as tortuosity.[50] For tubular inorganic membranes dedicated to tangential liquid filtration, the basic retention mechanism is based on the steric exclusion brought about by the effective separation layer. This latter must be as thin as possible to prevent a decrease in the diffusion flow below unacceptable values. Therefore this separation layer is always deposited

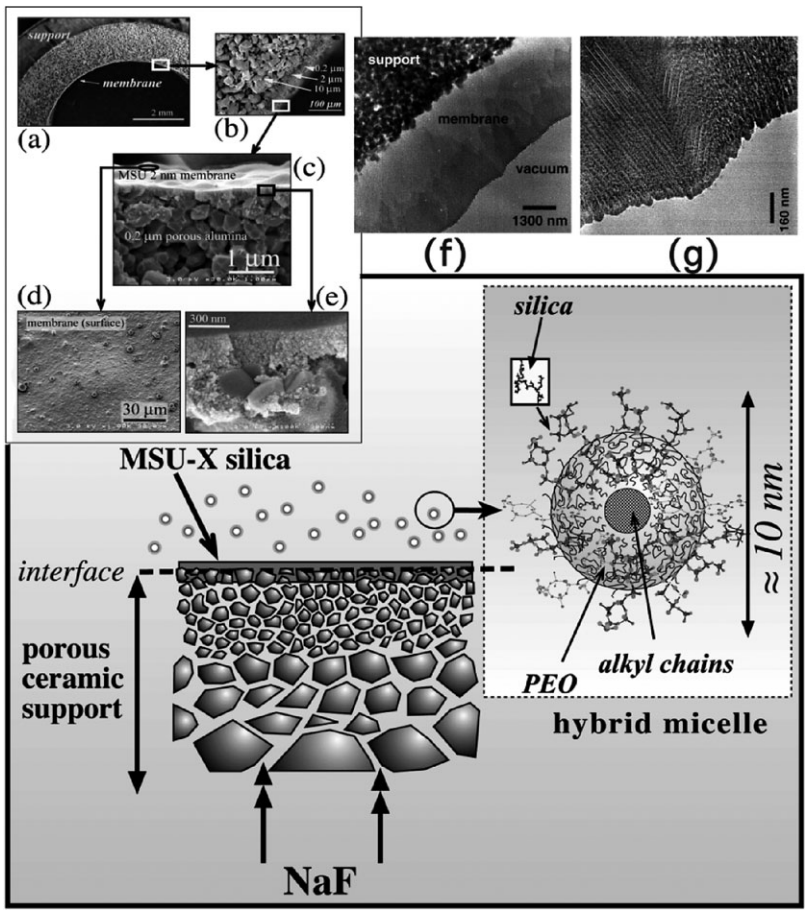

Fig. 11 Principle of the interfacial reaction involved for the synthesis of a mesoporous silica membrane from a solution of hybrid micelles. Insets: SEM micrographs of the tubular membrane; (a) cross section of the support: the silica membrane is synthesized onto the internal surface of the alumina support; (b) closer view of the support with three alumina layers that exhibit a decreasing pore size (10 µm, 2.0 µm. and 0.2 µm, respectively) from the external surface toward the internal one; (c) cross section of the membrane synthesized on the 0.2 µm porous alumina sublayer; (d) surface of the membrane; (e) close-up view of the interface between the silica membrane and the 0.2 µm porous alumina sublayer; (f) TEM micrograph of a cross-section of this membrane and (g) close-up view of the surface where parallel silica columns can be clearly identified.

onto one or several stacked macroporous layers that provide the mechanical strength required for easy handling. When the membrane exhibits very small pores (below 50 nm), an additional mechanism based on the superficial charge of the membrane itself will help or prevent charged species such as ions from diffusing through the membrane. This charge depends both on the nature of the filtration layer and on the pH of the filtered solution.[51] Separation properties of porous membranes are therefore governed by two main mechanisms: (i) membrane structure (pore size, morphology, tortuosity) and (ii) surface properties (charge, specific interactions), the latter becoming paramount as the pore size decreases. It appears from this description that an accurate control of the hierarchical structure of an actual membrane could enhance specific properties resulting from the topology of its porous network as well as from the surface properties that it could exhibit. We illustrated this concept by making a 2.5 nm pore diameter membrane from mesostructured silica. This silica is obtained by a self-assembly mechanism between hybrid micelles made of nonionic PEO-based surfactants and silicon alkoxides hydrolyzed at mild pH.[52] This synthesis is a two-step process that involves first the formation of hybrid micelles where a diffuse layer of silica (1 molecule for 30 molecules of water) surrounds the initial spherical micelle built with an inner hydrophobic core and an outer hydrophilic palisade of ethylene oxide chains (see inset in Fig. 11). These objects are stable and silica condensation will occur only if a catalyst like a fluoride ion is added, which constitutes the second step of this synthesis. This implies that a control can be exerted on the silica condensation, not only as a function of time (when is F^- ion added?) but also as a function of space (where is it added?). If a membrane is seen as a hierarchical object, these hybrid micelles constitute the basic bricks of it. We used a commercial tubular porous ceramic membrane as support. It is shown at different scales in Fig. 11 (a)–(e). A solution of stable hybrid micelles is circulating in the window of the membrane whereas an aqueous solution of sodium fluoride is allowed to diffuse from the outer of the ceramic support.[53] By this method, the formation of silica will occur only at the interface that corresponds to the inner surface of the ceramic support (see main scheme in Fig. 11 and photos (c) to (e)).

A continuous film of mesoporous silica is obtained. This continuity is very important because the fluid to filter must diffuse through the internal—structural—porosity in silica,

which requires the absence of any external—textural—porosity that would exist if the membrane were made of particles. Moreover, a close observation by TEM (Fig. 11, insets (f) and (g)) reveals that this interfacial reaction led to a global growth of mesoporous columns perpendicular to the porous substrate. It is noteworthy that lines observed in these pictures do not correspond to the actual porosity but to silica columns with a parallel alignment of pores. The rejection efficiency of the membrane was tested in filtration of polyethylene oxide polymers (PEO) in water as a function of pH (Fig. 12) (filtration pressure $\Delta P = 4$ bar, with PEO 600, 1000, 1500, 4000 and 10 000). It appears obviously that the retention rate is highly dependent on the pH, whatever the molecular weight of the PEO polymer. Indeed, an effective rejection is observed above pH 2 but it remains limited to 80% even with the biggest polymer. On the other side, a sharp drop of the rejection capacity appears below pH 2 (dotted vertical line), even for PEO 10 000 that presents a mean diameter of 6.8 nm, by far bigger than the 2.5 main pore diameter of the silica membrane.[54] This specific behavior (rejection rate limited to 80% and drop to zero for pH < 2) can be explained by the specific shape (non-connecting straight pores) and surface properties (pH-dependent charge of the silica surface) provided by the initial self-assembly of the hybrid micelles and their preferential growth perpendicular to the substrate support. The rejection threshold limited at 80%, whatever the polymer size can be understood by de Gennes' works on self-diffusion of non-adsorbing flexible, linear and branched polymers in nanopores.[55]

Taking into account some preliminary statements, two parameters were identified, which were (i) the potential self-diffusion of a polymer without flow in a straight pore and (ii) the determination of the critical flow that could make all polymers go through the pore. PEO polymer chains in water behave like statistical spherical coils swelled with water where their shape is the result of equilibrium between the natural stretching and entropic spring effects that leads to an average spherical shape. If this equilibrium is modified by an external parameter such as an adsorption strength or confinement, the PEO polymer ball will be subjected to strain and will adopt a new configuration. Fig. 12(a) displays a schematic of the interaction of a polymer coming into contact with a pore (1). Even without any flow, the polymer chain can theoretically move in and out of the pore (2). At this point, the polymer chain is better described as a series of spherical objects called "blobs" that contain a certain amount of monomers (here, $-CH_2-CH_2-O-$) and whose size is equal to the pore diameter (d) (see (A)(3) in Fig. 12). The number of monomers per blob can be calculated from the Flory law, based on the relationship [$gD = (D/a)^{5/3}$] where D is the pore diameter ($D \approx 2.5$ nm in our study), g is the number of monomers per sphere and a the length of a CH_2-CH_2O monomer ($a \approx 0.37$ nm).[56] For example, PEO 600 is small enough to enter the pore entirely as a single undistorted blob whereas PEO 10 000 must be described as a short chain of four spherical blobs, once entered into the pore. When the polymer enters partially into the pore, it is subjected to a confinement that creates a force tending to pull the chain out of or through the pore. This force will allow the polymer to "crawl" inside the pore and non-zero permeation coefficients are calculated, which depend on the polymer size (the permeation coefficient is 4 times bigger for PEO 600 than for PEO 10 000).[54] This phenomenon is perfectly illustrated by our membrane which

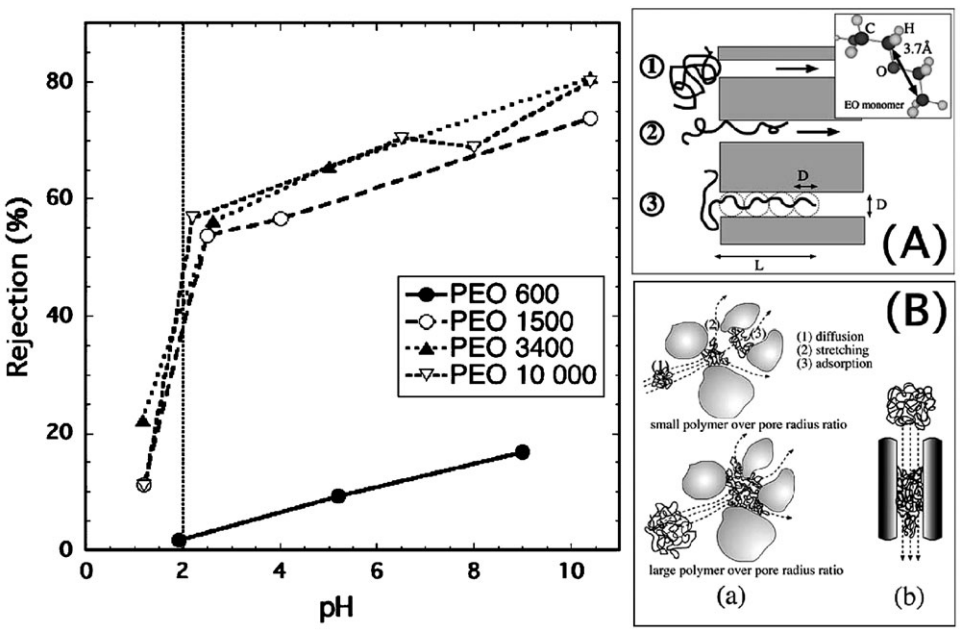

Fig. 12 Evolution of the rejection rate of the silica mesoporous membrane as a function of the pH of the solution, for different PEO polymers. Whereas above pH 2 one finds the expected behavior of inorganic membranes, below pH 2 one observes a drastic decrease of the rejection rate, whatever the size of the polymer. (A): Scheme of polymer diffusion inside a nanopore: (1) polymer at the entrance of the pore, (2) diffusion inside the pore, (3) description of the polymer as a chain of globular "blobs". Inset: length of a $-(CH_2-CH_2-O)-$ monomer. (B): Differences in the diffusion of polymer inside (a) a classical inorganic membrane obtained by the controlled stacking of colloidal particles, which leads to a highly connected porous framework and (b) the silica mesoporous membrane exhibiting tubular pores.

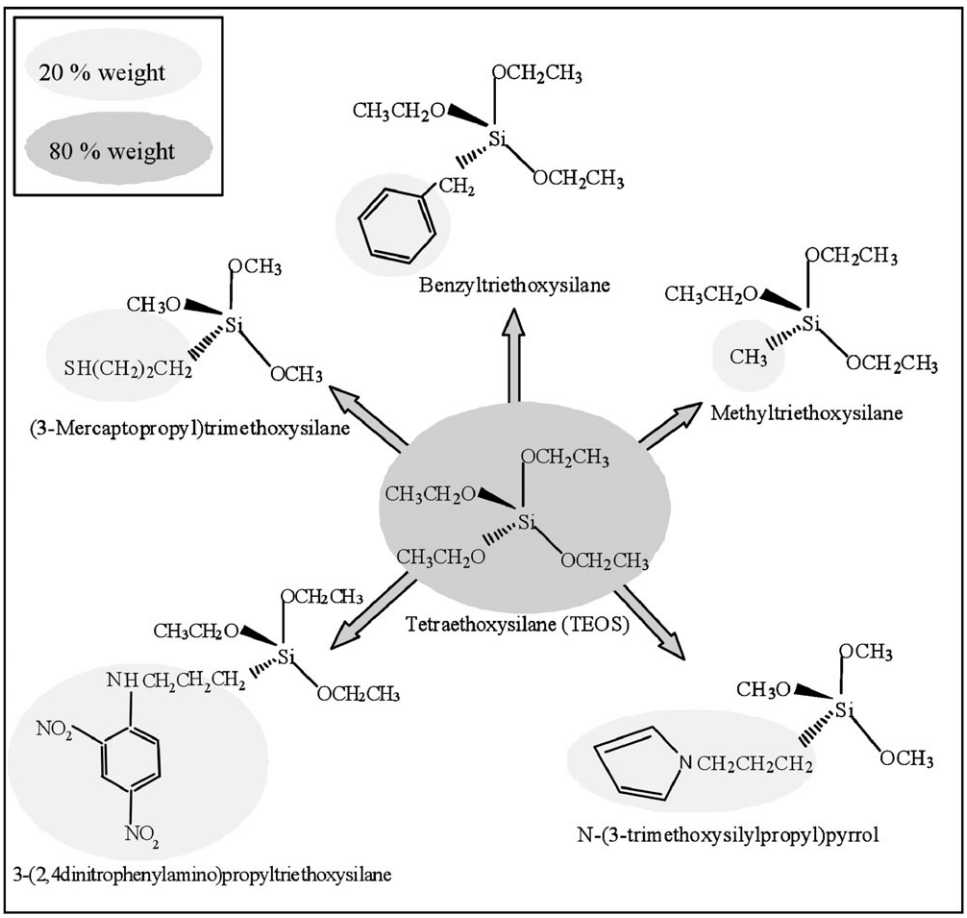

Fig. 13 Different organosilanes mixed with TEOS as precursors. Final porous silica-based materials have been labelled, benzyl-Si(HIPE), mercapto-Si(HIPE), dinitro-Si(HIPE), pyrrole-Si(HIPE) and methyl-Si(HIPE) (ref. 65, copyright 2007 American Chemical Society).

constitutes a direct example of the theoretical works of de Gennes *et al.* Diffusion of all polymers under flow into a straight pore with no specific interactions will occur above a critical flow.[57] The required values of flow are too high compared with our experiment, which explains why the membrane has an effective retention power towards polymers and that only self-diffusion through straight pores is the limiting factor that prevents the retention rate from reaching a 100% value even with PEO 10 000. This self-diffusion can be observed only if there are straight non-connecting pores. Indeed, normal membranes are made by particles stacking (see Fig. 11b), giving a tortuous porous network that blocks the diffusion of polymers through it.[58] A comparison is displayed in Fig. 12(b). However, self-diffusion of polymers cannot explain the sharp decrease of retention beyond pH 2, even for the biggest polymers. Interactions between PEO chains and silica have long been known and depend on interactions between the oxygen atoms of the PEO chains and the silica surface. Therefore an additional parameter regarding the adsorption of PEO polymers onto the silica surface must be taken into account in this case. The oxygen atoms of the PEO chains bear a negative partial charge at pH 7 ($\delta = -0.44$).[59] The silica charge itself is highly dependent on the acidity of the solution: below pH 2, the silica exhibits a positive charge, with $Si–OH_2^+$ groups on its surface, whereas above pH 2, silica adopts a neutral, then increasing negative surface charge with $Si–O^-$ surface groups. Above pH 2, the polymers can be seen as "non-adsorbing" and the mechanism described by de Gennes applies. On the contrary, below pH 2, interactions can occur between the oxygen of the PEO chains and the silica surface. This electrostatic interaction, which must be weakened by the solvent effect, is certainly not strong enough to allow a high strain on the polymer but it should help to conform the polymer in a way that helps hydrogen bonding between the $–Si–OH_2^+$ surface sites of the silica and the polymer oxygen atoms. Its main consequence is the induction of a switch in polymer conformation between freely moving polymer balls (above pH 2) and trains of adsorbed polymers in a semi-diluted regime (below pH 2).[60] This drastic change in the diffusion regime explains the steep drop in the retention rate since polymers can distort thanks to this interaction, enter the pore and then diffuse through it with the 4 Pa applied pressure as the driving force without being blocked since the self-assembly process led to straight non-connecting pores.

Example of meso-macrocellular foams obtained through emulsification process

Ordered macro-mesoporous materials are of interest for multiple applications in heterogeneous catalysis, separation

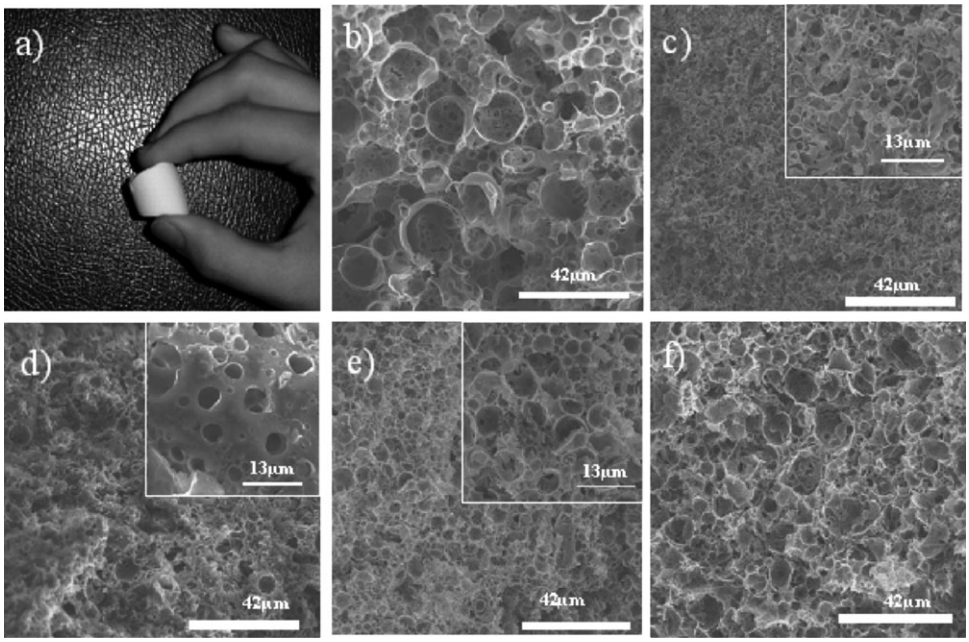

Fig. 14 (a) Photograph of one of the as-synthesized organo-Si(HIPE) monoliths obtained (pyrrole-Si(HIPE)). SEM micrographs: (b) pyrrole-Si(HIPE), (c) methyl-Si(HIPE), (d) dinitro-Si(HIPE), (e) benzyl-Si(HIPE), and (f) mercapto-Si(HIPE) (ref. 63, reproduced by permission of the Royal Society of Chemistry).

techniques, absorbers, sensors, optics *etc*. One way of generating such architectures is to use either direct concentrated non-aqueous[61] or aqueous emulsions.[62] With this aim, our research group has developed a new process to obtain macrocellular silica monoliths with a high control over the final macroscopic cells (size and morphology) by adjusting the oil volume fraction of concentrated direct emulsions. This new series of silica porous networks were labelled Si(HIPE)[63] in reference to the first generation of porous organic polymers obtained through the use of concentrated reverse emulsions, porous polymers named polyHIPE, ''high internal polymeric emulsion'' phases.[64] More recently we developed for the first time a one-step method to prepare hybrid organic–inorganic porous silica-based monoliths bearing a bimodal porous structure where a hierarchical architecture is triggered by the combination of a direct water/oil concentrated emulsion on the macroscopic scale and a supramolecular surfactant organization on the mesoscopic scale.[65] Functionalization that makes the use of a co-condensation (''one-pot'') process where the entity (R-Si(OEt)$_3$) is incorporated in the reaction medium and participates in the whole synthesis has been investigated for providing optimized properties and new functionalities to these multi-scale organized structures (Fig. 13). In order to incorporate functionalities into the final materials we added different organically-modified silanes as well as tetraethoxyorthosilane (TEOS). A 20% and 80% weight ratio of these molecular species were, respectively introduced in the starting emulsion.

On the macroscopic length scale, pattern takes advantage of the concentrated direct emulsion, *i.e*. dispersion of oil in water, where the continuous phase will be the hydrophilic medium containing the hydrolyzed precursors. When condensation is advanced and the monoliths are dried, a further thermal treatment at 180 °C is applied in order to both ''remove'' the organic solvents and consolidate the inorganic walls. It is important to obtain monolith-type materials (Fig. 14a) since it usually indicates interconnected macroporosity (Fig. 14b–f). The first observation emerging from Fig. 14b–f is that the macroscopic void spaces are not monodisperse in size but rather polydisperse, ranging from 5 μm up to 30 μm.

The macroscopic textures of the monoliths resemble to an ''hollow spheres'' aggregation, except for the material dinitro-Si(HIPE). As previously used to generate Si(HIPE)0.035, the high acidic concentration yields the silica far from its isoelectric point and therefore the native object will depict a strong Euclidean character. When using amino groups as is the case for the (2,4-dinitrophenylamino)propyltriethoxysilane entities with the same HCl concentration, the pH will increase closer to the silica isoelectric point and the final walls will be associated with a more fractal character, where the continuous aqueous medium will be fully mineralized. Beyond SEM observation, mercury porosimetry has been performed on these supports (not shown here). The first piece of information that is of importance for further applications is the fact that these as-synthesized materials possess mechanical strength high enough to support mercury impregnation. As previously observed for the inorganic Si(HIPE) series, we obtain two sets of windows. First we have the windows that intrinsically connect two adjacent macropores, previously called ''internal junctions''.[63] Also, considering the aggregated ''hollow spheres'' textural aspect of the macropores, we have to consider windows emerging from aggregation between several hollow spheres; this is what we have previously called ''external junctions''. On the other hand, the macropore distribution becomes narrower when considering the material dinitro-Si(HIPE), as the continuous aqueous phase is more completely mineralized and the aggregated ''hollow sphere'' character is practically lost (Fig. 14d), for the reason explained above, *i.e*.

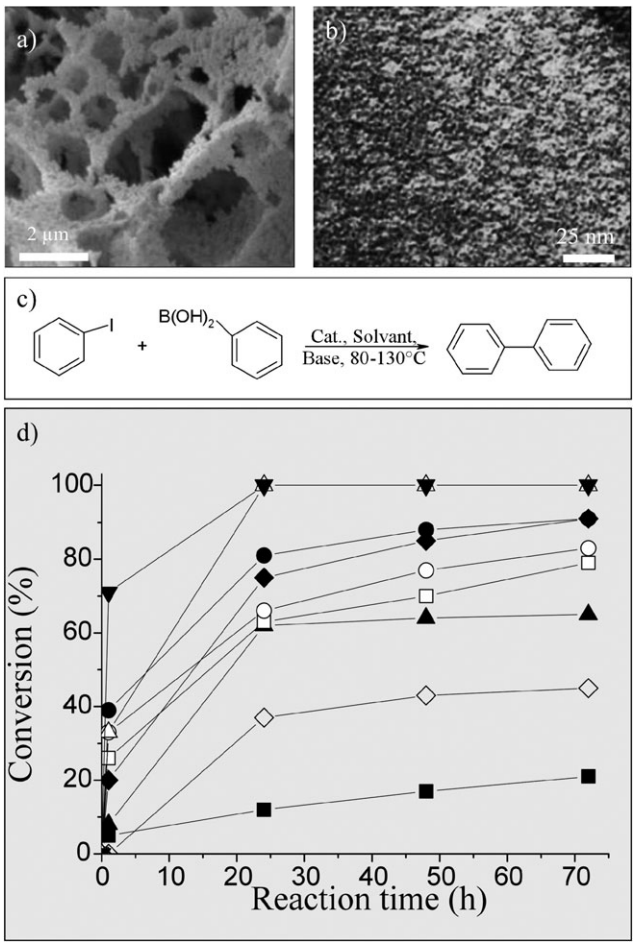

Fig. 15 (a) SEM picture of a conventional polyHIPE, (b) TEM picture of ED–P2 at high magnification, (c) Suzuki–Miyaura coupling reaction, (d) catalytic conversion *versus* time for the Suzuki coupling of iodobenzene and phenylboronic acid using different catalyst: ◇ ED–P4; △ $Pd(PPh_3)_4$ (homogeneous catalysis); ○ Pd/C; □ ED; ▲ PA–P4; ● PA–P2; ■ PA; ◆ ED–P2; ▼ PA–P2 (powder). Three kind of functions have been grafted onto the polymeric supports, namely: an ethylenediamine $–NHCH_2CH_2NH_2$, (labelled ED), a primary amine $–NH_2$ (labelled as PA). P2 and P4 indicate that the molar ratios triphenylphosphine (PPh_3)/Pd are, respectively, 2/1 and 4/1. In this study, we chose to work with PPh_3 as co-stabilizing agent because this molecule is known to strongly bind to palladium and to form stable complexes (ref. 66*b*, copyright 2005 Wiley-VCH).

the walls have enhanced fractal character. At the mesoscopic length scale these hybrid organic–inorganic porous monoliths possess a secondary porosity. This mesoporosity can be first observed using TEM investigations, qualitatively studied using SAXS experiments and quantified with nitrogen physisorption measurements that reveal porosity ranging from 50 to 400 $m^2\ g^{-1}$.[65] Microscopic FTIR spectroscopy demonstrates that the organosilane moieties remain intact through the synthesis while ^{29}Si-NMR shows that the average degree of condensation for these hybrid networks ranges between 86 and 90% yielding shaped monoliths with both good integrity and sufficient mechanical properties to be usable as functional catalytic or chromatographic supports.

Previously to this one step "co-condensation process" we synthesized a series of Pd@polyHIPE[66] and Au@polyHIPE[67] compounds where the support matrices are made of macroporous polystyrene/divinylbenzene. In particular, the Pd@polyHIPE materials were obtained using a three-step synthetic route: (i) synthesis of the organic macroporous matrix, (ii) functionalization of the support surface by various organic groups (ethylene diamine, primary amine) and (iii) *in situ* generation of palladium nanoparticles. The activities of the obtained catalysts Pd@polyHIPE toward a Suzuki–Miyaura coupling reaction have revealed good potential when compared to classical catalytic supports such as Pd/C when used in conjunction with PPh_3 (triphenylphosphine) as soluble additive.[66*b*] In particular, the supports obtained by grafting ethylene diamine present good activity towards a wide variety of substrates, even those known to be poorly reactive such as aryl chloride (Fig. 15).

Remarkably, considering the Fig. 15, the catalyst PA–P2 presents a better activity than Pd/C commercial available catalysts, while still employed under a monolith form. When this support is crushed with a mortar, the reaction kinetics are largely improved and present an activity comparable to that of the homogeneous $Pd(PPh_3)_4$. On the other hand, the polymer supports suffer from both high temperature reaction and the hexane solvent employed during the catalysis reaction, thereby not achieving high cycling catalytic performance. This is the reason why current efforts are made to extend this work to silica-based hierarchical hybrid networks using the same stabilizing agent, leading to the new series of Pd@organo-Si(HIPE) compounds.[68] The catalytic properties of these hybrid materials, limiting the Pd content for the Mizoroki–Heck reaction,[69] are reaching turnover numbers (TON) and turnover frequencies (TOF), respectively, equal to 2961 and 141 h^{-1}.[68] The values obtained, if similar with the ones reported[70] on heterogeneous catalysis of Mizoroki–Heck reaction performed with powdered compounds, are certainly among the highest ever reached for porous monolith-type matrices.[71]

Conclusion and perspectives

Herein through the generation of one-dimensional (1D), bi-dimensional (2D) or tri-dimensional (3D) complex architectures, we demonstrate the ability of Integrative chemistry to scissor condensed matter on several length scales, in view of reaching final enhanced applications. In this general context, beyond bio-inspired materials, Integrative chemistry appears as an interdisciplinary new concept for the design and construction of complex architectures. Its main principle is to offer us a full set of tools where integration between inorganic, organic and supramolecular chemistry and the physical chemistry of complex fluids allows both specifying and enhancing final material functionalities according to what induced morphologies are desired, and not *vice versa*.

Considering the materials presented here and elsewhere,[4,6,7] we note that they bear a double hierarchy, hierarchy in their final textures and also a hierarchy regarding their mode of construction. First they are structurally hierarchically organized, but considering the shaping modes used, they are also subject to a hierarchy considering the strength addressed through their shaping process. For instance cohesion at the

microscopic length scale is promoted through strong interaction (covalent or iono-covalent bonds), whereas cohesion at the interface between the microscopic network and the mesoscopic one, or even within the mesoscopic template, will be weaker, (electrostatic or ionic interactions), while the organization on the macroscopic length scale is even weaker and is generally induced through the appliance of external stimuli (shear rate, mechanical dip-coat, electric field and so forth).

Integrative chemistry indeed offers the possibility for chemical science and physics to construct complex architectures with a strong "rational design", where the actual synthetic pathways employ construction modes (or reactors) that will act with cooperative modes of action (or a continuous mode of action) over all length scales. These strategies will better feature the construction modes that nature likely uses to build complex architectures. Indeed, natural materials and biological organisms are constituted of complex and hierarchical skeletons, but the shaping modes and the cohesion strengths are not hierarchically digressive, they are both continuous and certainly cooperative from the micro- to the macroscopic length scale.

The second challenge of integrative chemistry will be certainly to create complex architectures while saving energy, atoms and cost, thus achieving a certain pragmatism and reaching the idea of "green chemistry".[9]

Overall, we believe that optimism and creativity certainly remain the first factors to bear in mind when considering the new trend of integrative chemistry as an "interdisciplinary tool box".

References

1. G. M. Whitesides and R. F. Ismagilov, *Science*, 1999, **284**, 89.
2. (*a*) S. Mann, *Angew. Chem., Int. Ed.*, 2000, **39**, 3392; (*b*) G. A. Ozin, H. Yang and N. Coombs, *Nature*, 1997, **386**, 692; (*c*) S. Mann and G. A. Ozin, *Nature*, 1996, **382**, 313.
3. (*a*) G. A. Ozin, *Chem. Commun.*, 2000, **6**, 419; (*b*) I. Soten and G. A. Ozin, *Curr. Opin. Colloid Interface Sci.*, 1999, **4**, 325; (*c*) G. A. Ozin, H. Yang and N. Coombs, *Nature*, 1997, **386**, 692.
4. (*a*) S. Mann, in *Biomimetic Materials Chemistry*, ed. S Mann, Wiley-VCH, Weinheim, 1997, pp. 1; (*b*) *Biomimétisme et Matériaux (Arago 25)*, ed. C Sanchez, OFTA, Paris, 2001, vol. 25; (*c*) P. Calvert, in *Biomimetic Materials Chemistry*, ed. S Mann, Wiley-VCH, Weinheim, 1997, pp. 315; (*d*) *Biomimetics: Design and Processing of Materials*, ed. M Sarikaya and I Aksay, AIP, Woodbury, CT, 1995; (*e*) C. Sanchez, H. Arribart and M. M. Giraud-Guille, *Nat. Mater.*, 2005, **4**, 277; (*f*) E. Bäuerlein, *Angew. Chem., Int. Ed.*, 2003, **42**, 614; (*g*) S. Weiner and H. D. Wagner, *Annu. Rev. Mater. Sci.*, 1998, **28**, 271; (*h*) M. M. Giraud-Guille, *Int. Rev. Cytol.*, 1996, **166**, 59; (*i*) A. Peytcheva and M. Antonietti, *Angew. Chem., Int. Ed.*, 2001, **17**, 3380; (*j*) B. Bensaude-Vincent, H. Harribart, H. Boulignand and C. Sanchez, *New J. Chem.*, 2002, **1**, 1.
5. (*a*) *Hierarchical Structures in Biology as a Guide for New Materials Technology*, ed. D. A. Tirrell, National Material Advisory Board, The National Academic Press, Washington, DC, 1994, pp. 1–130; (*b*) K. Kenichi, F. Kazushi, S. Junzo and S. A. Kazunari, *Langmuir*, 2002, **18**, 3780.
6. (*a*) S. Mann, S. L. Burkett, S. A. Davis, C. E. Fowler, N. H. Mendelson, S. D. Sims, D. Wals and N. T. Whilton, *Chem. Mater.*, 1997, **9**, 2300; (*b*) G. J. A. A. Soler-Illia, C. Sanchez, B. Lebeau and J. Patarin, *Chem. Rev.*, 2002, **102**, 4093.
7. (*a*) R. Backov, *Soft Matter*, 2006, **2**, 452; (*b*) E. Prouzet, Z. Khani, M. Bertrand, M. Tokumoto, V. Guyot-Ferreol and J.-F. Tranchant, *Microporous Mesoporous Mater.*, 2006, **1–3**, 369; (*c*) C. Sanchez, C. Boissière, D. Grosso, C. Laberty and L. Nicole, *Chem. Mater.*, 2008, **3**, 682.
8. R. Backov, *Actual. Chim.*, 2009, awaiting publication.
9. P. T. Anastas and J. C. Warner, in *Green Chemistry Theory and Practice*, Oxford University Press, New York, 1998.
10. (*a*) G. Percin and B. T. Khuri-Yakub, *Rev. Sci. Instrum.*, 2003, **74**, 1120; (*b*) M. Mougenot, M. Lejeune, J. F. Baumard, C. Boissière, F. Ribot, D. Grosso, C. Sanchez and R. Noguera, *J. Am. Ceram. Soc.*, 2006, **6**, 1876.
11. J. Zeleny, *Phys. Rev.*, 1914, **3**, 69.
12. L. Larrondo and R. Manley, *J. Polym. Sci., Polym. Phys. Ed.*, 1981, **19**, 909.
13. (*a*) C. M. Lieber, *MRS Bull.*, 2003, **28**, 486; (*b*) Y. N. Xia and P. D. Yang, *Adv. Mater.*, 2003, **15**, 351; (*c*) M. S. Sander, A. L. Prieto, R. Gronsky, T. Sands and A. M. Stacy, *Adv. Mater.*, 2002, **14**, 665.
14. (*a*) C. L. Dennis, R. B. Borges, L. D. Buda, U. Ebels, J. F. Gregg, M. Hehn, E. Jouguelet, K. Ounadjela, I. Petej, I. L. Prejbeanu and M. J. Thorntorn, *J. Phys.: Condens. Matter*, 2002, **14**, R1175; (*b*) Y. Henry, K. Ounadjela, L. Piraux, S. Dubois, J. M. George and J. L. Duvail, *Eur. Phys. J. B*, 2001, **20**, 35.
15. (*a*) D. Li and Y. Xia, *Adv. Mater.*, 2004, **16**, 1151; (*b*) Y. Dzenis, *Science*, 2004, **304**, 1917; (*c*) A. L. Yarin, S. Koombhongse and D. H. Reneker, *J. Appl. Phys.*, 2001, **89**, 3018; (*d*) E. Zussman, A. Theron and A. L. Yarin, *Appl. Phys. Lett.*, 2003, **82**, 973; (*e*) W. Sigmund, J. Yuh, H. Park, V. Maneeratana, G. Pyrgiotakis, A. Daga, J. Taylor and J. C. Nino, *J. Am. Ceram. Soc.*, 2006, **89**, 395; (*f*) H. Wu, D. Lin and W. Pan, *Appl. Phys. Lett.*, 2006, **89**, 133125; (*g*) D. Li, Y. Wang and Y. Xia, *Nano Lett.*, 2003, **3**, 1167; (*h*) M. Peng, D. Li, L. Shen, Y. Chen, Q. Chen, Q. Zheng and H. J. Wang, *Langmuir*, 2006, **22**, 9368; (*i*) D. Li, T. Herricks and Y. Xia, *Appl. Phys. Lett.*, 2003, **83**, 4586.
16. Z. Huang, Y. Zhang, M. Kotaki and S. Ramakrishna, *Compos. Sci. Technol.*, 2003, **63**, 2223.
17. H. Wu, R. Zhang, X. Liu, D. Lin and W. Pan, *Chem. Mater.*, 2007, **19**, 3506.
18. S. Chikazumi, *Physics of Magnetism*, John Wiley & Sons, New York, 1964, ch. 1, pp. 19.
19. (*a*) X. H. Yan, G. J. Liu, M. Haeussler and B. Z. Tang, *Chem. Mater.*, 2005, **17**, 6053; (*b*) X. H. Yan, G. J. Liu, F. T. Liu, B. Z. Tang, H. Peng, A. B. Pakhomov and C. Y. Wong, *Angew. Chem., Int. Ed.*, 2001, **40**, 3593; (*c*) N. A. Burker, H. D. Stover and F. P. Dawson, *Chem. Mater.*, 2002, **14**, 4752.
20. D. Jiles, *Introduction to Magnetism and Magnetic Materials*, Chapman and Hall, London, 1991, ch. 1, pp. 91.
21. (*a*) D. Weller and A. Moser, *IEEE Trans. Magn.*, 1999, **35**, 4423; (*b*) L. Sun, C. L. Chien and P. C. Searson, *Chem. Mater.*, 2004, **16**, 3125; (*c*) D. L. Leslie-Pelecky and R. D. Rieke, *Chem. Mater.*, 1996, **8**, 1770; (*d*) J. A. Barnard, H. Fujiwara, V. R. Inturi, J. D. Jarratt, T. W. Scharf and J. L. Weston, *Appl. Phys. Lett.*, 1996, **69**, 2758.
22. (*a*) L. Biette, F. Carn, M. Maugey, M.-F. Achard, J. Maquet, N. Steunou, J. Livage, H. Serier and R. Backov, *Adv. Mater.*, 2005, **17**, 2970; (*b*) H. Serrier, M.-F. Achard, O. Babot, N. Steunou, J. Maquet, J. Livage, C. M. Leroy and R. Backov, *Adv. Funct. Mater.*, 2006, **16**, 1745; (*c*) C. M. Leroy, N. Steunou, L. Binet, M.-F. Achard, P. Masse, J. Livage and R. Backov, *Chem. Mater.*, 2007, **19**, 3988.
23. B. Vigolo, A. Pénicaud, C. Coulon, C. Sauder, R. Paillet, C. Journet, P. Bernier and P. Poulin, *Science*, 2000, **290**, 1331.
24. (*a*) J. Livage, *Chem. Mater.*, 1991, **3**, 578; (*b*) O. Pelletier, P. Davidson, C. Bourgaux, C. Coulon, S. Regnault and J. Livage, *Langmuir*, 2000, **16**, 5295; (*c*) B. Vigolo, C. Zakri, F. Nallet, J. Livage and C. Coulon, *Langmuir*, 2002, **18**, 9121.
25. (*a*) G. Micocci, A. Serra, A. Tepore, S. Capone, R. Rella and P. Siciliano, *J. Vac. Sci. Technol., A*, 1997, **15**, 34; (*b*) J. Liu, X. Wang, Q. Peng and Y. Li, *Adv. Mater.*, 2005, **17**, 764.
26. M. T. Anderson, J. E. Martin, J. Odinek and P. Newcomer, in *Microporous and Macroporous Materials*, ed. R. F. Lobo, J. S. Beck, S. L. Suib, D. R. Corbin, M. E. Davi, L. E. Iton and S. I. Zones, Materials Research Society, Pittsburgh, 1996, vol. 431, pp. 217.
27. (*a*) G. Ogawa, *Chem. Commun.*, 1996, 1149; (*b*) G. Ogawa, *J. Am. Chem. Soc.*, 1994, **116**, 7941.
28. (*a*) H. Yang, A. Kuperman, N. Coombs, S. Mamiche-Afara and G. A. Ozin, *Nature*, 1996, **379**, 703; (*b*) H. Yang, N. Coombs and G. A. Ozin, *J. Mater. Chem.*, 1998, **8**, 1205.

29. (*a*) Y. Lu, R. Ganguli, C. A. Drewien, M. T. Anderson, C. J. Brinker, W. Gong, Y. Guo, H. Soyez, B. Dunn, M. H. Huang and J. I. Zink, *Nature*, 1997, **389**, 364; (*b*) C. J. Brinker, Y. Lu, A. Sellinger and H. Fan, *Adv. Mater.*, 1999, **11**, 579; (*c*) C. J. Brinker, *MRS Bull.*, 2004, **29**, 631; (*d*) C. Boissière, D. Grosso, H. Amenitsch, A. Gibaud, A. Coupe, N. Baccile and C. Sanchez, *Chem. Commun.*, 2003, 2798.
30. (*a*) E. L. Crepaldi, G. J. A. A. Soler-Illia, D. Grosso, P. A. Albouy and C. Sanchez, *Chem. Commun.*, 2001, 1582; (*b*) P. C. Angelome, S. Aldabe-Bilmes, M. E. Calvo, E. L. Crepaldi, D. Grosso, C. Sanchez and G. J. A. A. Soler-Illia, *New J. Chem.*, 2005, **29**, 59; (*c*) T. Brezesinski, M. Groenewolt, M. Antonietti and B. M. Smarsly, *Angew. Chem., Int. Ed.*, 2006, **45**, 781; (*d*) A. Cabot, J. Arbiol, A. Cornet, J. R. Morante, F. L. Chen and M. L. Liu, *Thin Solid Films*, 2003, **436**, 64; (*e*) T. Brezesinski, M. Groenewolt, N. Pinna, H. Amenitsch, M. Antonietti and B. M. Smarsly, *Adv. Mater.*, 2006, **18**, 1827; (*f*) D. Grosso, G. J. de A. A. Soler-Illia, F. Babonneau, C. Sanchez, P.-A. Albouy, A. Brunet-Bruneau and A. R. Balkenende, *Adv. Mater.*, 2001, **13**, 1085; (*g*) D. Grosso, C. Boissière, B. Smarsly, T. Brezesinski, N. Pinna, P. A. Albouy, H. Amenitsch, M. Antonietti and C. Sanchez, *Nat. Mater.*, 2004, **3**, 787; (*h*) G. J. D. A. Soler-Illia and C. Sanchez, *New J. Chem.*, 2000, **24**, 493; (*i*) P. D. Yang, T. Deng, D. Y. Zhao, P. Y. Feng, D. Pine, B. F. Shmelka, G. M. Whitesides and G. D. Stucky, *Science*, 1998, **282**, 2244; (*j*) Y. Sakatani, C. Boissière, D. Grosso, G. J. D. A. Soler-Illia and C. Sanchez, *Chem. Mater.*, 2008, **20**, 1049.
31. (*a*) S. H. Baeck, K. S. Choi, T. F. Jaramillo, G. D. Stucky and E. W. McFarland, *Adv. Mater.*, 2003, **15**, 1269; (*b*) K. S. Choi, H. C. Lichtenegger, G. D. Stucky and E. W. McFarland, *J. Am. Chem. Soc.*, 2002, **124**, 12402; (*c*) H. M. Luo, L. Sun, Y. F. Lu and Y. S. Yan, *Langmuir*, 2004, **20**, 10218; (*d*) T. Xue, C. L. Xu, D. D. Zhao, X. H. Li and H. L. Li, *J. Power Sources*, 2007, **164**, 953.
32. (*a*) K. J. Edler, *Soft Matter*, 2006, **2**, 284; (*b*) K. J. Edler and S. J. Roser, *Int. Rev. Phys. Chem.*, 2001, **20**, 387; (*c*) K. J. Edler, in *Handbook of Sol–Gel Science and Technology: Processing Characterization and Applications*, ed. S Sakka, Kluwer Academic Publishers, Norwell, MA, 2005, vol. 1, pp. 541.
33. Y. Yang, Y. F. Lu, M. C. Lu, J. M. Huang, R. Haddad, G. Xomeritakis, N. G. Liu, A. P. Malanoski, D. Sturmayr, H. Y. Fan, D. Y. Sasaki, R. A. Assink, J. A. Shelnutt, S. F. van, G. P. Lopez, A. R. Burns and C. J. Brinker, *J. Am. Chem. Soc.*, 2003, **125**, 1269.
34. (*a*) N. G. Liu, D. R. Dunphy, P. Atanassov, S. D. Bunge, Z. Chen, G. P. Lopez, T. J. Boyle and C. J. Brinker, *Nano Lett.*, 2004, **4**, 551; (*b*) N. G. Liu, Z. Chen, D. R. Dunphy, Y. B. Jiang, R. A. Assink and C. J. Brinker, *Angew. Chem., Int. Ed.*, 2003, **42**, 1731.
35. (*a*) J. D. Joannopoulos, R. D. Meade and J. N. Winn, *Photonic Crystals*, Princeton University Press, New York, 1995; (*b*) *Photonic Band Gap Materials*, ed. C. M. Soukoulis, Kluwer, Boston, MA, 1996; (*c*) A. Scherer, T. Doll, E. Yablonovitch, H. O. Everitt and J. A. Higgins, *J. Lightwave Technol.*, 1999, **17**, 1928 (special issue); (*d*) S. John, *Phys. Today*, 1991May), 32; (*e*) E. Yablonovitch, *J. Opt. Soc. Am. B*, 1993, **10**, 283; (*f*) J. D. Joannopoulos, P. R. Villeneuve and S. Fan, *Nature*, 1997, **386**, 143.
36. M. Madou, *Fundamentals of Microfabrication*, CRC Press, New York, 1997.
37. D. Philp and J. F. Stoddart, *Angew. Chem., Int. Ed. Engl.*, 1996, **35**, 1154.
38. L. V. Woodcock, *Nature*, 1997, **385**, 141.
39. P. Jiang, J. F. Bertone, K. S. Hwang and V. L. Colvin, *Chem. Mater.*, 1999, **11**, 2132.
40. A. Mihi, M. Ocana and H. Miguez, *Adv. Mater.*, 2006, **18**, 224.
41. M. Clemente-Leon, E. Coronado, C. J. Gomez-Garcia, C. Mingotaud, S. Ravaine, G. Romualdo-Torres and P. Delhaes, *Chem.–Eur. J.*, 2005, **11**, 3979.
42. S. Reculusa and S. Ravaine, *Chem. Mater.*, 2003, **15**, 598.
43. P. Massé and S. Ravaine, *Chem. Mater.*, 2005, **17**, 4244.
44. F. Garcia-Santamaria, H. Miguez, M. Ibisate, F. Meseguer and C. Lopez, *Langmuir*, 2002, **18**, 1942.
45. X. Ma, J. Q. Lu, R. S. Brock, K. M. Jacobs, P. Yang and X. H. Hu, *Phys. Med. Biol.*, 2003, **48**, 4165.
46. K. Wostyn, Y. Zhao, G. de Schaetzen, L. Hellemans, N. Matsuda, K. Clays and A. Persoons, *Langmuir*, 2003, **19**, 4465.
47. P. Massé, S. Reculusa, K. Clays and S. Ravaine, *Chem. Phys. Lett.*, 2006, **422**, 251.
48. R. D. Pradhan, I. I. Tarhan and G. H. Watson, *Phys. Rev. B: Condens. Matter Mater. Phys.*, 1996, **54**, 13721.
49. R. Rengarajan, P. Jiang, D. C. Larrabee, V. L. Colvin and D. M. Mittleman, *Phys. Rev. B*, 2001, **64**, 205103.
50. A. J. Burggraaf, in *Important Characteristics of Inorganic Membranes. Fundamentals of Inorganic Membrane Science and Technology*, ed. A. J. Burgraaf and L Cot, Elsevier Science, New York, 2000, vol. 4, pp. 21.
51. P. Fievet, A. Szymczyk, A. Aoubiza and J. Pagetti, *J. Membr. Sci.*, 2000, **168**, 87.
52. E. Prouzet and C. Boissière, *C. R. Chim.*, 2005, **8**, 579.
53. C. Boissière, M. A. U. Martines, P. J. Kooyman, T. R. de Kruijff, A. Larbot and E. Prouzet, *Chem. Mater.*, 2003, **15**, 460.
54. C. Boissière, M. A. U. Martines, A. Larbot and E. Prouzet, *J. Membr. Sci.*, 2005, **251**, 17.
55. P.-G. de Gennes, *Adv. Polym. Sci.*, 1999, **138**, 91.
56. P. Flory, *Principles of Polymer Chemistry*, Cornell Universary Press, New York, 1953.
57. C. Gay, P.-G. de Gennes, E. Raphaël and F. Brochard-Wyart, *Macromolecules*, 1996, **29**, 8379.
58. P. L. J. Zitha, G. Chauveteau and L. Leger, *J. Colloid Interface Sci.*, 2001, **234**, 269.
59. J. Livage, M. Henry and C. Sanchez, *Prog. Solid State Chem.*, 1988, **18**, 259.
60. J. Israelachvili, *Intermolecular and Surface Forces*, Academic Press, London, 1991.
61. A. Imhof and D. J. Pine, *Adv. Mater.*, 1998, **10**, 697.
62. G.-R. Yi and S. M. Yang, *Chem. Mater.*, 1999, **11**, 2322.
63. F. Carn, A. Colin, M.-F. Achard, H. Deleuze, M. Birot and R. Backov, *J. Mater. Chem.*, 2004, **14**, 1370.
64. D. Barby and Z. Haq, *Eur. Pat.* 0060138, 1982.
65. (*a*) S. Ungureanu, M. Birot, L. Guillaumme, H. Deleuze, O. Babot, B. Julian, M.-F. Achard, M. I. Popa, C. Sanchez and R. Backov, *Chem. Mater.*, 2007, **19**, 5786; (*b*) S. Ungureanu, H. Deleuze, C. Sanchez and R. Backov, *Mater. Res. Soc. Symp. Proc.*, 2007, **1007**, S04–06.
66. (*a*) A. Desforges, H. Deleuze, O. Mondain-Monval and R. Backov, *Ind. Eng. Chem. Res.*, 2005, **44**, 8521; (*b*) A. Desforges, R. Backov, H. Deleuze and O. Mondain-Monval, *Adv. Funct. Mater.*, 2005, **15**, 1689.
67. C. Féral-Martin, M. Birot, H. Deleuze, A. Desforges and R. Backov, *React. Funct. Polym.*, 2007, **67**, 1072.
68. S. Ungureanu, H. Deleuze, M. I. Popa, C. Sanchez and R. Backov, *Chem. Mater.*, submitted.
69. (*a*) T. Mizoroki, K. Mori and A. Ozaki, *Bull. Chem. Soc. Jpn.*, 1971, **44**, 581; (*b*) R. F. Heck and J. P. Nolley, Jr, *J. Org. Chem.*, 1972, **37**, 2320.
70. O. Aksin, H. Turkmen, L. Arto, B. Cetinkaya, N. Chaoyinj, O. Buyukgungor and E. Ozkal, *J. Organomet. Chem.*, 2006, **691**, 30227.
71. C. M. Cruddden, M. Satteesh and R. Lewis, *J. Am. Chem. Soc.*, 2005, **127**, 10045.